2010

Laser shockwave sintering of micro and nanoscale powders of yttria-stabilized zirconia

Victor Orlando Roa Baerga
Iowa State University

Laser shockwave sintering of micro and nanoscale powders of yttria-stabilized zirconia

by

Victor Orlando Roa Baerga

A thesis submitted to the graduate faculty

in partial fulfillment of the requirements for the degree of

MASTER OF SCIENCE

Co-majors: Mechanical Engineering, Electrical Engineering

Program of Study Committee:
Pal Molian, Co-major Professor
Liang Dong, Co-major Professor
Qingze Zou

Iowa State University

Ames, Iowa

2010

Dedication

This thesis is dedicated to my wife and son, Krista and Victor, without them I wouldn't be here today. Krista you have been with me every step of the way, through good times and bad. Thank you for your love, guidance, and support that you have always given me, helping me to succeed and instilling in me the confidence that I am capable of doing anything I put my mind to. My son Victor, no matter how frustrated or angry I was while I was writing, all I had to do was look at you and see that big warm smile on your face to cheer me up. Thank you both for always being there. I love you!

Table of Contents

List of Figures

List of Tables

Acknowledgement

I am very grateful for the opportunity to work on this project and the personal growth and knowledge I gained working on it. I have much gratitude and admiration to my major advisor Dr. Molian for his support and guidance in this project. His dedication to helping me succeed and constantly driving me to do better is something I will never forget.

Thank you to Liang Dong and Qingze Zou for supporting me by being a part of my program of study and reviewing my work.

Thank you to Larry Jones and Hal Sailsbury for allowing me to use their facilities and providing assistance to produce and test my samples.

Thank you to Xinwei Wang and his student Xiaopeng Huang for allowing me to use their lab and providing assistance in the thermal conductivity measurements of my samples.

Abstract

Mechanical (non-thermal) sintering behavior of yttria stabilized zirconia powder compact was investigated as a function of particle size. Cubic crystalline form of ZrO_2 containing 8 mole% Y_2O_3 powders of the nominal size 16 µm and 45 nm were acquired, cold pressed in a die to make green compacts and then subjected to a novel laser shock peening (LSP) process for densification. Results indicated that micropowder compacts (MC) excessively cracked and chipped while nanopowder compact (NC) and mixtures of micro/nanopowder compacts (MNC) underwent sintering without crack formation. However there was evidence of stress-assisted material removal and surface disruption in NC samples, making their surfaces much rougher than those of MC samples. In addition, MC exhibited a much higher increase in hardness over NC and MNC. A 64 % increase in hardness was obtained in MC compared to a 44 % increase in NC. Furthermore there was grain coarsening effect in NC and MNC as compared to MC. Overall an improved densification was obtained in NC and MNC samples.

Analytical model results indicated residual stresses occurring deeper in the material for MC compared to NC and validated the higher hardness obtained in the MC samples. The NC samples were subjected to higher plastic strain compared to the MC samples that led to more plastic deformation in the NC samples. The plastically affected depths for the samples indicate the penetration of the LSP process reached over 25% of the 1 mm thick compacts. Lowering the repetition rate from 5 to 3 Hz increases the pulse pressure, plastically affected depth and surface plastic strain by 4% for both MC and NC, while the surface residual stresses increased by 85% (MC) and 104% (NC).

We hypothesize that laser shock waves create a compressive stress pattern that causes plastic deformation of the particles and a large increase in the concentration of vacancies on the surface of the particles; this highly defective surface coupled with a high surface mobility of nanoparticles is responsible for the mass transport. In addition the strong bonding between nanoparticles and possible stress-assisted phase transition to monoclinic phase at the grain boundaries reduce significantly the pores thus resulting in a high density part. This hypothesis agrees with the results that were seen in the analytical model.

Thermal conductivity measurements indicate that the MNC have approximately half the thermal conductivity of the MC. The reduction in thermal conductivity in MNC is attributed to the presence of nanoparticles at the pores that limit the mean free paths of phonons and photons.

Chapter 1. Introduction

Laser shock peening (LSP) is a surface treatment process designed to improve the mechanical properties of materials which include hardness, fatigue life, and residual stress distribution (Zhang and Yao, 2001). LSP uses a high intensity (1-100 GW/cm^2) and short pulsed (1-50 ns) laser on the surface of the target material to generate a plasma (Dahotre and Harimkar, 2008). This plasma expands creating high pressure shockwaves that propagate through the target material and produce stresses much larger than the dynamic yield strength of the material (>1 GPa). Plastic deformation of the surface and formation of compressive residual stresses to a certain depth in the subsurface are the outcomes (Warren, Guo and Chen, 2008). By confining the plasma strongly, an increase in the generated pressure can be achieved. In order to confine the plasma, a transparent material such as water or glass must be used. Confining the plasma also results in longer duration shockwaves.

Using high intensity lasers directly on the target may result in damaging the surface of the material. Hence a thin protective absorbent coating or film (sacrificial material) on the target material must be applied to prevent the surface ablation. Black paint and aluminum foil are types of sacrificial materials generally used (Molian, Molian and Nair, 2009). The laser vaporizes this coating and creates the plasma. The plasma will be trapped between the transparent material and the target. The plasma will then expand upon further laser energy absorption, to induce extreme shockwaves propagating through the target material. Figure 1 schematically describes the LSP process.

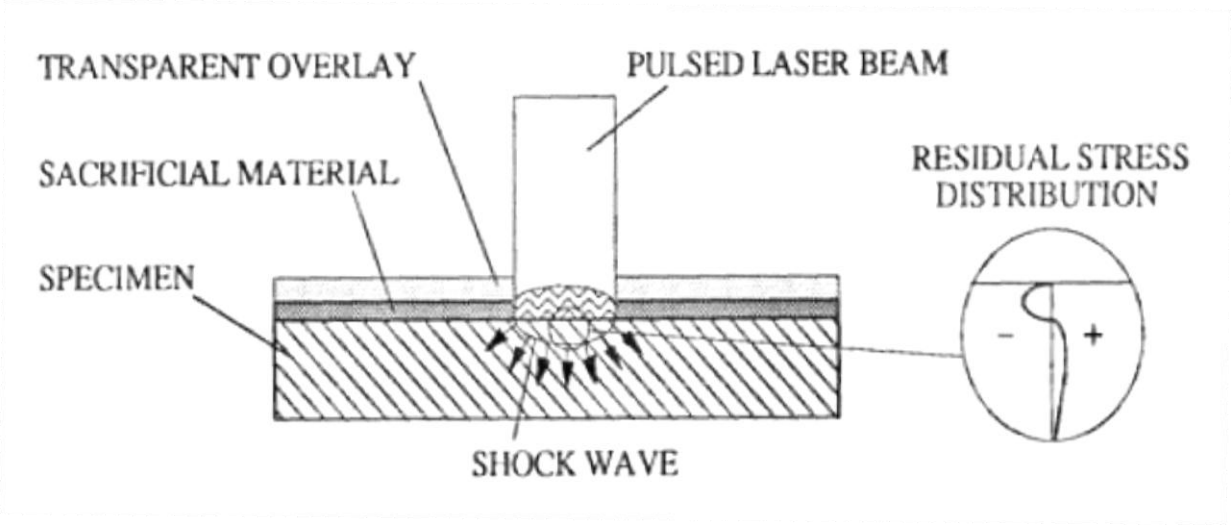

Figure 1. Schematic of the laser shock peening process (Unknown)

The thickness of the absorbent coating can influence the results; a thin coating can cause the thermal effects to be transferred to the target material while a thick coating can cause the attenuation of the shock waves (Dahotre and Harimkar, 2008). It may be noted the coating (paint, Al-foil, etc.) must be thin (<20 μm) with low heat of vaporization for the generation of high-amplitude stress waves. The presence of transparent overlay increases the ablation pressure by a factor 5 to 10 and an increase of shock duration by a factor of 2 to 3 compared to direct ablation (Boustie, Berthe, Resseguier and Arrigoni, 2008). However, the pressure may saturate above a threshold power density depending on the overlay medium, wavelength and pulse width (Montross *et al.*, 2002). Equations of state of materials, phase diagrams and dynamics are required to determine the true behavior of shock waves. One unique aspect of LSP is that high power pulsed lasers are the best among various shock generators to induce high amplitude pressures in extremely short time (Figure 2).

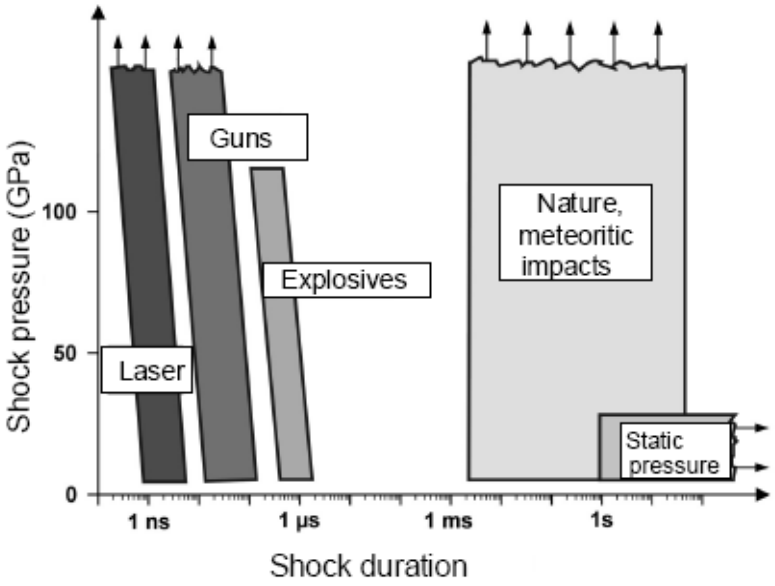

Figure 2. Various shock generators (Boustie *et al.*, 2008)

An increase in fatigue strength is accomplished by the creation of large magnitudes of compressive residual stresses which develop in the subsurface and increase hardness. The maximum compressive residual stress is often formed at the surface of the target material and decreases in magnitude with increasing depth below the surface. Using larger spot sizes allow shockwaves to propagate deeper into the material and increasing the depth of plastic deformation (Warren *et al*., 2008). The transient shock waves can also induce microstructure changes (dislocations, vacancies, grain size and phase transformations) near the surface and cause high density of dislocations to be formed. The combined effect of the microstructure changes and dislocation entanglement contribute to an increase in the mechanical properties in the near surface (Zhang and Yao, 2002). However these properties are not very uniform. By creating massive LSP zones and controlled peening spacing, an improvement in uniformity can be achieved. It may

also prove effective to perform multiple LSP passes in order to create larger magnitudes of residual stresses and hardness (Warren *et al*., 2008). Figure 3 shows the simulation created by Warren's group that indicates increasing the laser intensity increases both the stress magnitude and affected depth. Also, using smaller laser spot sizes decreases the largest magnitude of residual stress and decreases the depth affected by LSP. Larger spot sizes have less energy attenuation and cause more plastic deformation.

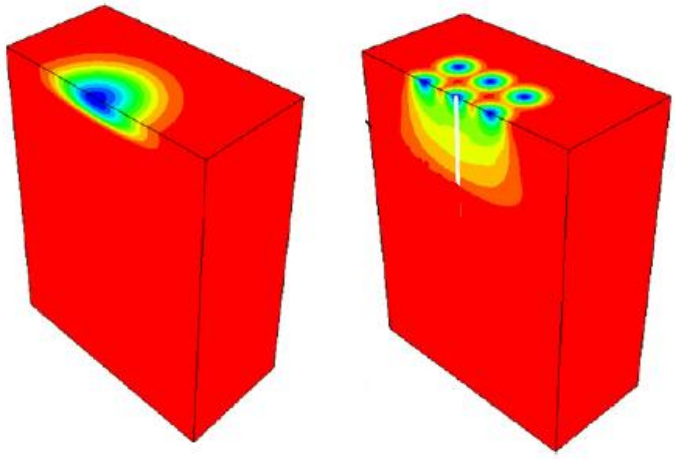

Figure 3. Simulation model of single and massive parallel LSP (Warren *et al*., 2008)

The applications of laser shock waves are primarily in cleaning, hardening (to improve fatigue strength), sheet metal bending and changing the surface microstructure, stress state and morphology of materials and parts (Dubrujeaud and Jeandin, 1994; Warren *et al*., 2008; Zhang and Yao, 2002; Zhang, Yao and Noyan, 2004). For example, Yao's group reported microscale effects of laser shock waves to obtain the desired residual stress patterns in microcomponents such as MEMS microgears (Zhang and Yao, 2002; Zhan *et al*., 2004). *In the area of powder sintering, LSP has not been studied*

although it is less cumbersome and safer than explosive shock processing that uses dangerous explosives and plate acceleration to consolidate the powders.

1.1 Problem Statement

The purpose of this research effort is to investigate the effect of the laser shock peening process in micro and nanosized powder compacts of yttria-stabilized zirconia. Unlike traditional thermal sintering, the mechanical consolidation of powder compact by LSP is expected to produce high quality performance parts.

1.2 Research Objectives

Current research in LSP is essentially focused on the metallic alloys. Limited work has been reported on LSP of ceramics such as silicon nitride (Kruusing, 2004). Ceramics by virtues of higher strength and lower thermal conductivity over metal alloys are becoming the common materials in the industry. LSP has significant potential in improving both these properties of ceramics. Additionally no work has been reported on the use of LSP for mechanical sintering of ceramic powder compacts. Powders are generally used for coating applications; however, using them in a compact form allows the direct effects of LSP to be studied. Finally the size effect of powders on the mechanical consolidation is not available.

The hypothesis of our approach is harnessing the intense energy of laser shock waves to result in sintering of ceramic powders at room temperature (without extra heating). Hence the research objectives of the thesis are:

1. Demonstrate the feasibility of LSP for sintering of the YSZ powder compacts

2. Compare the sintering behavior of microscale and nanoscale powders of YSZ
3. Develop an analytical model to predict the plastically affected depth, residual stress and plastic strain on the surface as a result of shockwave propagation
4. Determine the changes in strength and thermal conductivity of powder compacts as a result of LSP

Significance: The proposed LSP technology has strong potential to transform the way YSZ parts are currently fabricated and can make quantum leap advances in the state-of-the-art densification. It will outperform the existing thermal sintering techniques which are inherently limited by the grain growth and precipitation. On the science front, our modeling will provide an improved fundamental understanding of laser shock waves to bind nanoparticles and cause phase transition. On the technology front, the process innovations will offer simplicity and robustness for sintering of YSZ at room temperature.

Chapter 2. Background

2.1 Laser Shock Peening

A significant amount of LSP research has been conducted on metal alloys including steels, aluminum alloys, titanium alloys, nickel-base superalloys, cast irons and powder metallurgy iron alloys. This research usually includes a study of residual stresses, fatigue and other material properties that are significantly affected by laser-induced shockwaves. In most LSP processes, laser beams are produced by a Q-switched laser system based on neodymium-doped glass or yttrium aluminum garnet (YAG) crystal lasing rod, which operates in the near infrared, having a wavelength of 1.064 μm and a pulse duration of 10-100 ns (Ding and Ye, 2006).

A review of LSP conducted on different metal alloys and materials is displayed in Tables 1 and 2 where a wide range of process parameters were employed. The most important parameters in these experiments are power density (GW/cm^2) and pulse duration (ns). The power densities of some of the experiments are incredibly high, producing a large amount of energy in a small area. The wavelength of the laser is also a very important parameter because it controls the interaction between the laser beam and the material surface (Ding and Ye, 2006).

Table 1. Processing parameters for laser shock processing of metals (Montross *et al.*, 2002)

Treated materials	Laser type	Laser power (J)	Power density (GW/cm^2)	Pulse duration (ns)	Laser beam size (mm)	Absorbent coating	Transparent overlay	Pressure (GPa)
Zn, Al	Nd:glass	500	1	20–40		Lead, zinc, black paint (8–10 μm)	Quartz or water (0.3 cm)	10
Fe–3wt%Si	Nd:glass	500	0.1–1	25–200		Lead	Quartz	
5086-H32, 6061-T6	Nd:glass	500	1.13–4.39, 1.34–2.16	25	1–3.0, 1.6–2.0		Quartz	2–6
2024-T351, 2024-T851, 7075-T631, 7075-T73	Nd:glass			20–30	6–30	Black paint	Quartz or water	
2024-T3	Nd:glass	200	4.4–12	13–18	11.4–16.3	Aluminum coated plastic	Quartz	
2024-T62	Nd:glass	18, 23	1.57, 7.32		6, 8	Black paint (0.1 mm)	K7 glass (4.5 mm)	
Hadfield steel	Nd:glass	100	2.4×10^3	~0.6	3–3.5	Black paint (40–50 μm)	None	~2
316L stainless steel	Nd:glass	80	300	0.6	7.5	Black paint	None	18
55C1 steel, 316L stainless steel	Nd:glass		1–8		4–5	Al paint Al adhesive	Water	2.7–6
316L stainless steel, X12CrNi12-2-2 steel	Nd:glass	40	8–9	8–10	3–4	Al foil, Al adhesive or paint	Water	5.5–6
Al–12Si, A356 Al, 7075	Nd:glass	80	1–8	15–30	5–12		Water (2–5 mm)	2.5
Fe–30%Ni	KDP	4000	10^2–10^4	1	25	No	None	
304 stainless steel	Nd:glass		2×10^3–2×10^3	0.6	3–6	Black paint	None	15–60
18Ni(250) steel	Nd:YAG	0.03	1×10^3	0.1	0.1	Black paint (~0.1mm)	Water (~3.5 mm)	
SAE1010 steel	Nd:glass	5–200	120–4700	0.6	3.0–3.5	Black paint (40–50 μm)	None	<2.5

Table 2. Typical laser systems used for LSP processes (Ding and Ye, 2006)

Treated materials	Laser type	Laser power (J)	Power density (GW/cm^2)	Pulse duration (ns)	Laser spot size (mm)	Absorbent coating	Transparent overlay	Peak pressure (GPa)
Rock	Nd: glass	5–100	1–15	20	2–6.6	–	Water	1.4
Al foil	Nd: glass	40	0–25	25–30	3–5	–	Water (glass)	5.5
Thin Al	Nd: YAG	6	0.05–1	150	3	–	–	0.8
Al 2024-T351 and T851, 7075-T631 and T73	Nd: glass	–	–	20–30	0.6–3	Black paint	Water (quartz)	10
2024-T3 Al	Nd: glass	–	5	18	10	Black paint	Water	–
2024-T62 Al	Nd: glass	–	1.57–7.32	18–23	6–8	Black paint	K7 glass	–
Al-12Si, A356 Al, 7075Al	Nd: glass	80	1–8	15–30	5–12	Black paint	Water	2.5
Ti-6Al-4V	Nd: glass	–	5.5–9	–	5.6	Black paint	Water	–
SUS304 s.	Nd: YAG	0.1	4.5	5	0.75	–	Water	0.5
316L s.s.	Nd: glass	40–100	8–20	3–10	–	Black paint	Water	10
Al, 55C1 s., 316L s.s.	Nd: glass	40	8–10	8–10	3–4	Al paint	Water	6
316L s.s., X12CrNi12-2-2 s.	Nd: glass	40–100	1–100	0.6–30	0.5–1	Al foil, Al adhesive	Water	6
Hypoeutectoid s.	Nd: glass	80	5–10	25	5	Black paint	Water (BK7 glass)	5
Fe-30%Ni Al	KDP	4000	10^3–10^4	1	4.3–25	–	–	0.6
304 s.s.	Nd: glass	80	300	0.6	7.2	Black paint	Water	18
Hadfield manganese	Nd: glass	100	2400	0.6	3–3.5	Black paint	Quartz	39.5
18Ni(250) s.	Nd: YAG	0.03	1000	0.15	0.1	Black paint	Water	–

Different types of absorbent coatings and transparent overlays can be used as shown in Tables 1 and 2. Absorbent coatings include black paint, aluminum, zinc and lead. The optical absorption and thermal properties of these coatings influence the peak pressure during confined ablation as shown in Figure 4. It may be noted that coatings with lower thermal conductivity (Zinc compared to Aluminum) generate higher peak pressures when the laser power density is less than 10^9 W/cm^2. At higher laser power densities (>4 x 10^9 W/cm^2) the peak pressure is driven by other dominant mechanism

such as the breakdown of the confining medium (Dahotre and Harimkar, 2008); this study, however, did not take into account using water as a confining medium and black paint as a coating. Black paint is one of the primary coatings currently being used in most LSP research as indicated in Table 1. Water tends to be a favorable confining medium for eliminating the thermal effects induced by the laser beam (Warren *et al*., 2008).

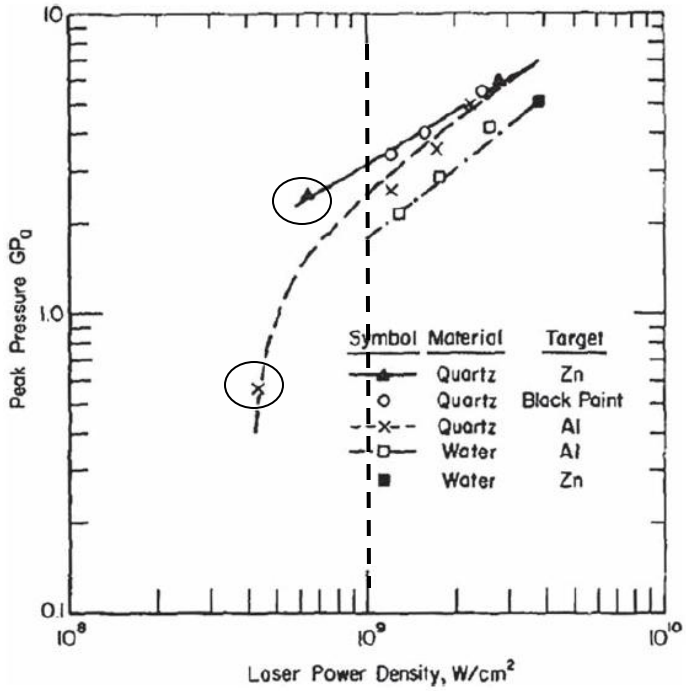

Figure 4. Variation of plasma induced peak pressures (Dahotre and Harimkar, 2008)

Water is the most common, cheap and safe medium among several liquids. The advantages of water over glass include: higher plasma pressure due to confinement; convection/explosive evaporation that carries debris away; efficient cooling of the work piece due to its exceptional heat capacity; and reduced atmospheric pollution. The

drawbacks of water are: water condensation on the nearby lens; light scattering by the water surface, suspensions and bubbles; energy loss due to absorption; harmful chemical reactions such as corrosion of material; photolysis; and hazardous to motion tables.

One of the central issues in using water is that it should not absorb much light. Figure 5 shows the transmission spectrum of water. Absorption length is based on Beer–Lambert law in which $I_x = I_o \exp(-x/\Delta)$ where I_o is the entrance light intensity, I_x is the light intensity at distance x and Δ is the light absorption length. It can be seen from Fig.5 that water is most transparent in the green light region obtained with frequency doubled Nd:YAG (also Nd:YFL) laser at 532 nm and copper vapor laser (CVL) at 511 nm.

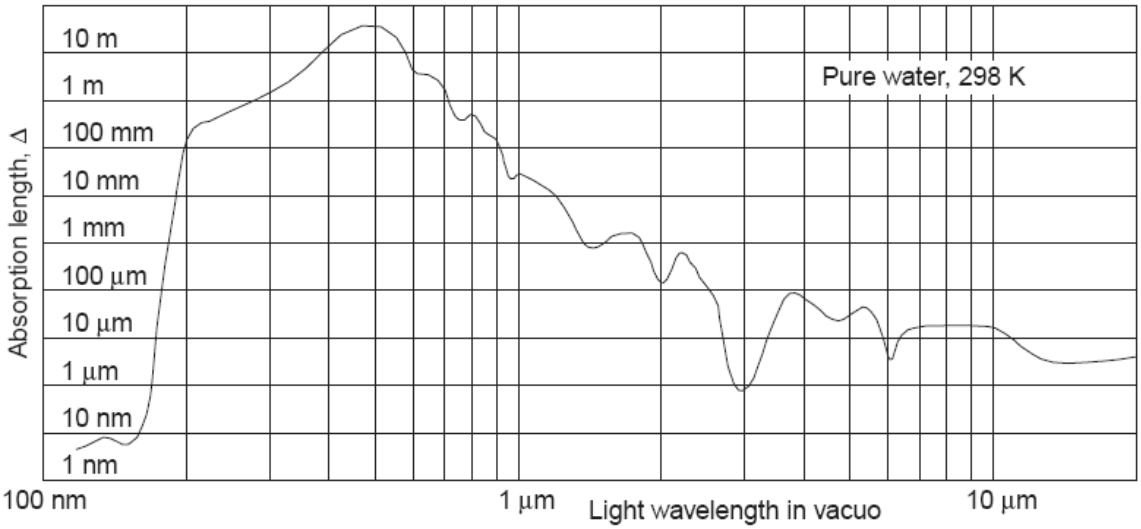

Figure 5. Transmission spectrum of laser light in water as a function of wavelength (Kruusing, 2004)

The three most common wavelengths used in LSP are 1064 nm (near infrared), 532 nm (green) and 355 nm (ultraviolet). Near infrared has only a modest absorption

coefficient in water overlay and moderate interaction with the metal surface, but a high dielectric breakdown threshold. While the 532 nm wavelength has the lowest absorption in water, its laser pulse energy output is reduced by a factor of two or more due to generating of the wavelength with harmonic single crystals (Warren *et al*., 2008). The 355 nm wavelength enhances shock wave generation due to the strong photon-metal interactions causing the power density threshold for dielectric breakdown to decrease, which limits the peak pressure. Dielectric breakdown reduces the energy available to generate a shockwave (Warren *et al*., 2008). The decrease in the dielectric breakdown threshold in a water-confining medium as a function of wavelength is displayed in Figure 6. Maximum peak pressures developed are approximately 4.5 to 5.5 GPa.

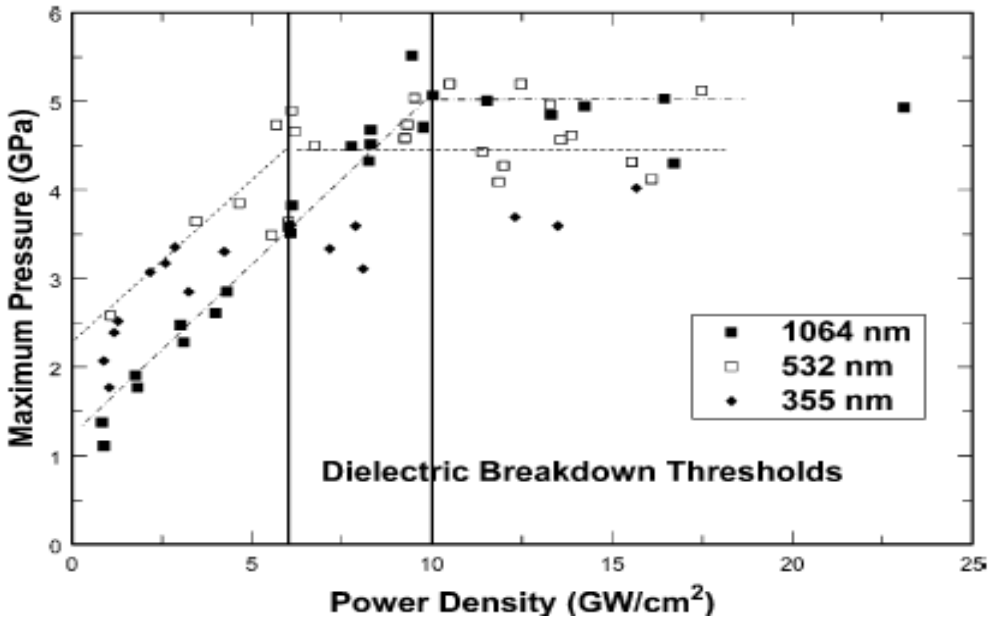

Figure 6. Peak pressure developed in LSP process as a function of power density and wavelength in water-confining medium (Montross *et al.*, 2002)

LSP can be performed individually or simultaneously on any surface of a thick alloy component. However, the laser pulse must be split to impact simultaneously on opposite sides for a thin section. This is done to balance the impact forces on the thin section in order to prevent the creation of a dimple on the irradiated side and a bulge on the opposite when the section is subjected to one-sided LSP. Also, spalling and fracture can occur if the strong enough shockwaves are produced. Two-sided LSP is used to treat thin metal alloys typically found on military aircraft and spacecraft (Ding and Ye, 2006). The two-sided LSP process is displayed in Figure 7.

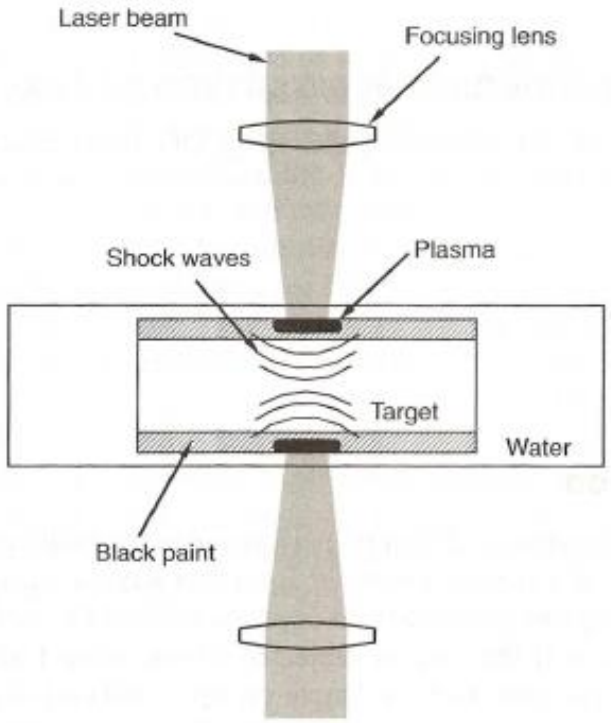

Figure 7. Two-sided LSP on a thin section (Ding and Ye, 2006)

Recent developments in LSP are high-energy and excimer lasers. Lawrence Livermore National Laboratory (LLNL) has developed fast-firing Q-switched Nd:glass lasers which deliver 200 J pulses with 20 ns pulse lengths at pulse rates of 10 Hz. Although this delivery rate is 20 times faster than currently available commercial systems, the costs and reliability do not justify for commercial acceptability. It should also be noted that ultraviolet excimer gas lasers (193-355 nm) are currently being developed to meet the demands of rapid shock peening of large area components by increasing their output energies.

Microscale Laser Shock Processing (μLSP) can impart compressive residual stress in Micro Electromechanical Systems (MEMS) components through laser-induced plasma and pressure pulse for improving fatigue performance and wear resistance (Che *et al*., 2009). Che's research group investigated μLSP on Al material using a shorter wavelength of 248 nm from an excimer laser with beam sizes of 20-200 μm for FEM simulation and laser irradiation experiments. Characteristic features studied include: plastic deformation, residual stress and microhardness. Che's research group used laser energies of 408 mJ (3.58 GW/cm^2) and 550 mJ (4.93 GW/cm^2) with a pulse duration of 20 ns (Che *et al*., 2009). Results showed that pulse energy, pulse number and thickness of coating layer are the main factors influencing the deformation depth (Che *et al*., 2009). Finally, larger stresses are produced from increasing the beam diameter that led to 35% increase in the maximum hardness over one laser irradiated area (Che *et al*., 2009).

The physical processes responsible for laser shock processing have been investigated both theoretically and experimentally by many researchers (Montross *et al.*, 2002; Kruusing, 2004; Warren *et al*., 2008). Physics of plasma generation (transmitted

power, generated pressures, expansion of plasma) in air and water are presented. In addition, simple 1D to very elegant 3D models have been presented that predict plasma pressure, thickness and velocity for a given laser power density and the material's acoustic impedances. Many properties including residual stress distribution are validated with these models. Figure 8 summarizes the events that take place during LSP.

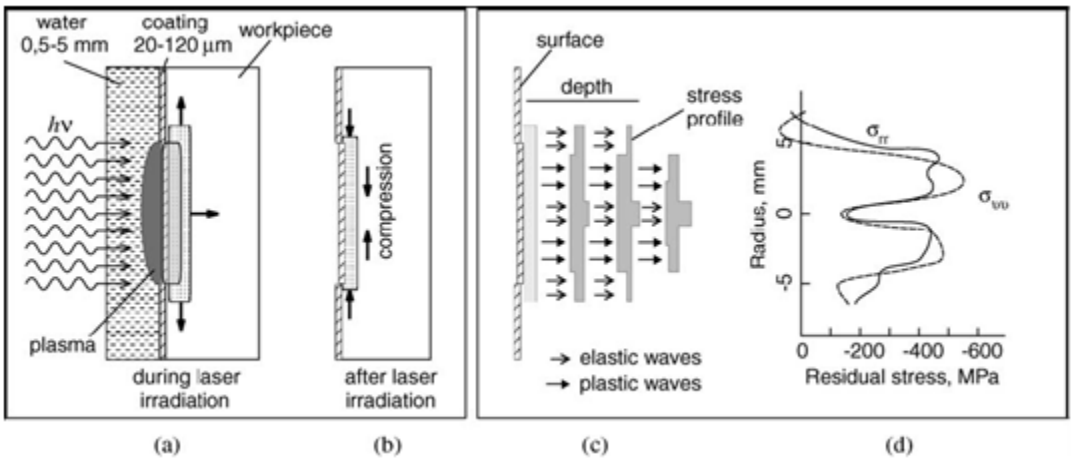

Figure 8. (a, b) Principle of laser shock processing in water confinement; (c) Schematics of shock wave motion under the irradiated area; (d) Experimental distribution of surface residual stresses in the work piece (Kruusing, 2004)

The main purpose of LSP is to change the microstructure and stress state of the material without melting or ablation. This is typically achieved by using single short laser pulses (nanoseconds) of high intensity and protective layers on the work piece. Many investigations have been performed on the surface morphology of LSP materials using SEM observations and roughness measurements. If the absorptive coating is absent then the process induces severe surface melting and vaporization in metals, leading to very

rough surfaces. Even with the absorptive coating there is an increased roughness. LSP creates significant microstructural changes by creating dislocations, causing phase transition and inducing plastic deformation. A higher dislocation density results in higher surface hardness and strength while plastic deformation reduces porosity and produces compressive surface stresses. In addition there is a potential for fine grain structure through phase transition. Experimental data indicates that the dislocation density is increased substantially in LSP aluminum alloys and low carbon steels (Montross *et al*., 2002). Furthermore, investigations of the effect of LSP on the weld zones in 18Ni (250) maraging steel revealed the phase transition from austenite to martensite. Numerous twins as well as α-phase were found in LSP of 316L stainless steels. The majority of the reports on microstructural changes have been qualitative and there is significant room for investigating the fundamental understanding on the interaction of the microstructure with laser induced shock waves.

Laser shock peening is mainly applied to metal alloys. However, new research is being conducted where metal alloys are being coated with micro and nano powders. This has proven to be successful with aluminum being coated with nanodiamond powders (Molian *et al*., 2009). This research compared using different wavelengths, confining mediums and absorbent coatings on aluminum 319 coated with nanodiamond powders. When using different confining mediums, water resulted in almost twice the microhardness than using glass. Using a water-confining medium and black paint resulted in the highest microhardness value of 1100 kg_f/mm^2. Finally, 532 nm wavelength resulted in a slightly larger microhardness value compared to 1064 nm. This research group

showed that LSP could generate a strong, wear resistant, durable carbon coating using nanodiamond powders (Molian *et al*., 2009).

Previous research shows that nanopowders can be effectively used in LSP (Molian *et al*., 2009); however, limited research has been conducted using micropowders. Also, no studies have been conducted using micro and nano powders in bulk compacts. LSP is a constantly growing field and new areas are continually being investigated. Every research group has at least shown some improvement in the mechanical properties of different types of metals. However, no studies have been shown to limit LSP only to metals or coatings. Different types of non-metallic materials should be researched in order to explore the benefits of LSP.

2.2 Nanomaterials

Nanomaterials such as nanopowders, nanotubes, nanowires and quantum dots exhibit unique mechanical (strength, modulus and toughness), electronic (bandgap, electrical resistivity), optical (light emission) and physical (density, thermal expansion, thermal conductivity) properties (Gutsch *et al*., 2004). For example, 25 nm TiO_2 particles which are transparent in the visible range are able to block the UV light effectively when compared to 250 nm particles (Zhao, Boxman and Chowdry, 2003). The superior properties of nanomaterials are attributed to their large surface areas, restricted vibrations of surface atoms, absence of electron scattering, changes in bond energy, particle size smaller than mean free path and wavelength of light, confinement and tunneling effect, small residual pore size, and extremely fine grain, phase, and domain size.

The important nanoparticulate materials are metal oxides such as SiO_2, TiO_2, Al_2O_3, Fe_2O_3, ZnO, CeO_2 and ZrO_2 (Elsevier, 2010; Marburger and Kvamme, 2005; Zhao *et al*., 2003). A variety of methods including spray pyrolysis, wet chemical synthesis, vapor phase condensation, rapid thermal decomposition of precursors in solution, sputtering, plasma reactors, flame and furnace reactors, sol-gel, and laser ablation are available to synthesize nanopowders. While SiO_2 and Fe_2O_3 nanoparticles have a commercial history spanning half a century or more, other oxides have recently entered into the marketplace. Nanopowders have proven their values by enhancing environment (catalytic converters), improving energy performance (fuel cells), extending Moore'law (single electron devices) and advancing healthcare (drug delivery). The largest application of nanotechnology is nanomaterials (about 40%) in the fields of electronics, biomedical, functional materials, human safety and environmental protection, and consumer and diversified products with a total world market of an estimated one billion dollar.

The two major challenges facing nanomaterials are: 1) manufacturing and 2) health and worker safety. In *manufacturing*, the key issues are assembling the nanoparticles without aggregation and agglomeration to produce the devices. The *societal problems* of nanopowders include health, worker safety and education, and public misunderstanding. Nanoparticles can have hazardous effects to the environment and worker health (skins, lungs and brain) as well as to the users through inhaling and ingesting. Unfortunately, the toxicology of nanomaterials has not been thoroughly evaluated under environmental and occupational exposure conditions.

A nanopowder is indeed a physical mixture of individual particles of less than 100 nm, clusters, aggregates and various levels of agglomerates due to the presence of unsaturated bonds on their surfaces and van der Waals bonding between crystallites. Figure 9 shows the three forms typically found in zirconia nanopowders (Kim, 2004). The individual nanoparticles are usually identified using TEM while the composite grains (clusters of single crystals) can be revealed most clearly by TEM but also by SEM. A loosely held cluster of composite grains is called an agglomerate which is on the order of few microns and can be readily seen by Optical Microscopy (OM).

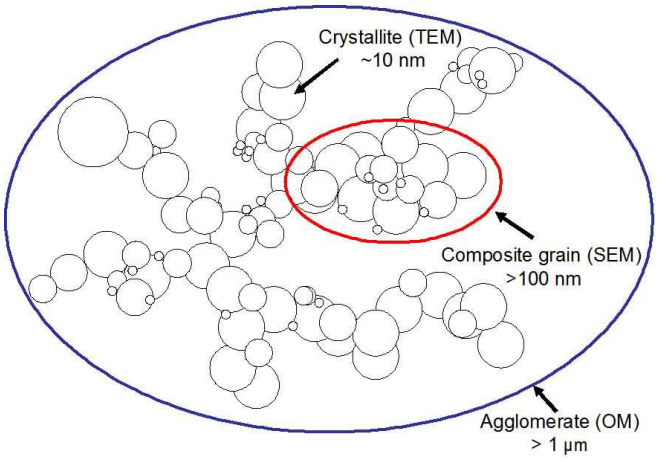

Figure 9. Constituents of a typical nanopowder (Kim, 2004)

2.3 Yttria stabilized zirconia and its properties and applications

Zirconium oxide, also referred to as zirconia or ZrO_2, is a high-temperature ceramic material with temperature capability up to 2400°C. It exhibits good chemical properties and exceptional electrical properties. The Zr^{+4} ions in the c-ZrO_2 structure are very immobile and therefore the diffusion coefficient of Zr^{+4} is small, resulting good

resistance to both acids and alkalis. In contrast, the O^{-2} ions are extremely mobile, making the cubic phase to be ion-conducting. ZrO_2 offers chemical and corrosion inertness to electric furnace heaters over 2000°C in oxidizing atmospheres. Pure ZrO_2 has three polymorphic forms that include monoclinic, tetragonal and cubic. The monoclinic is stable below about 1000°C. When the temperature is increased to above 1000°C but below 2300°C, tetragonal phase forms. Above 2300°C, the cubic form becomes stable. Pure zirconia is not quite useful for structural or mechanical applications because the transition from tetragonal to monoclinic during cooling from high-temperature is accompanied by a 3 to 5 percent volume increase leading to extensive cracking. Several oxides such as Y_2O_3, MgO and CaO which dissolve in the zirconia crystal structure can slow down or eliminate this phase change, leading to improved toughness. Thus, the addition of Y_2O_3, in the range of about 3 to 10 mole percent to zirconia, called yttria-stabilized zirconia or YSZ, can retain the tetragonal (partially stabilized) or cubic phase (fully stabilized) at room temperature. The addition of Y_2O_3 enhances the stability range of the cubic phase.

YSZ is a solid solution of ZrO_2 and Y_2O_3. Beyond about 7.5 mole% Y_2O_3, cubic form of YSZ is stable from room temperature to its melting point. This stabilization prevents the large volume expansion associated with the tetragonal to monoclinic phase change. The phase stability boundaries are also affected by particle size. It is known that a small particle size can stabilize the cubic phase of YSZ. The microstructures consist of coarse grains together with an intergranular glass phase that consists of various impurities added during the manufacturing process, but mainly SiO_2.

The typical properties of fully stabilized YSZ are: density 6000 kg/m^3, flexural strength 900 MPa, Young's modulus 200 GPa, Vicker's hardness 1300 kg/mm^2, and fracture toughness 13 MPa m$^{1/2}$ (Accuratus, 2005). YSZ has the lowest thermal conductivity of all ceramics at elevated temperatures because of its high concentration of point defects (oxygen vacancies and substitutional solute atoms), which scatter heat-conducting phonons (lattice waves) (Hass, 2000; Klemens, 1993). In addition, it has very high thermal expansion coefficient (Figure 10). Thermal conductivity of YSZ is lower than pure zirconia because yttria additions require the creation of O^{2-} vacancies to maintain the electrical neutrality of the ionic lattice. Thermal conductivity can further be reduced by engineering the microstructure and porosity and adding other rare-earth oxides which essentially generate phonon scattering defects.

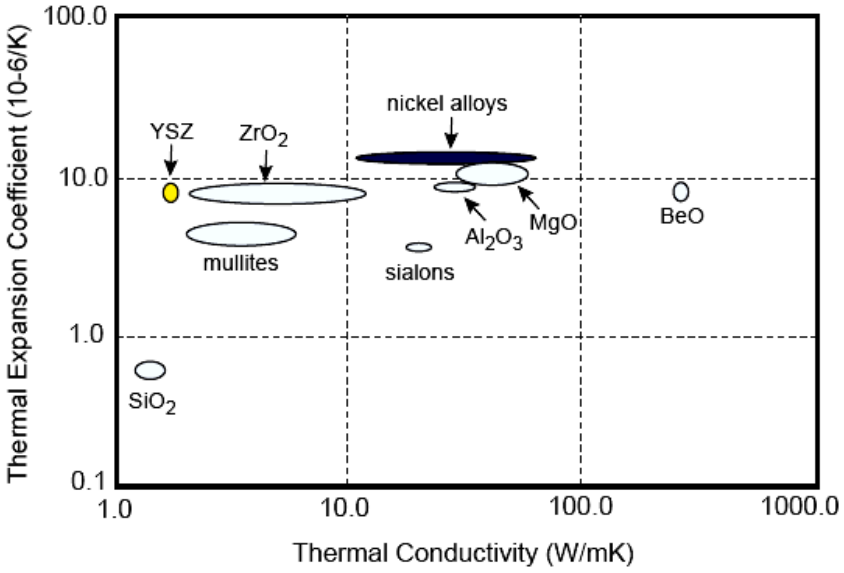

Figure 10. Thermal properties of ceramics (Klemens, 1993)

Yttria-stabilized zirconia (YSZ) is used in a wide range of industrial applications, e.g. as solid electrolytes in gas sensors or solid oxide fuel cells. This is because of their high oxygen conductivity due to the high concentration of oxygen vacancies and their good mechanical strength. It is also used as the susceptor (heater) in high temperature induction furnaces, luminescent displays, refractory linings, thermal barrier coatings, rollers and guides for metal tube forming, thread and wire guides and hot metal extrusion dies.

2.4 Thermal Sintering of YSZ

Thermal sintering is widely used to make YSZ parts. Typically zirconia powders are sintered in the temperature range of 1500°C-1700°C. During sintering, the bulk density of the ceramic increases as the powder compact shrinks due to a reduction in pore size and volume. Sintering is used interchangeably with densification although sintering is rigorously defined as "a process of densification driven by interfacial energy." Densification increases the contact area between adjacent particles, resulting in the generation of grain boundaries. The reduction in surface energy associated with the loss of surface area is the driving force to form a neck between adjacent particles. Essentially the migration of vacancies via surface diffusion is responsible for the neck formation in solid state densification (SSD). However SSD is slow and hence liquid phase sintering (LPS) with the use of an additive is used to perform rapid densification of the ceramic powders. The additive will melt and fuse the ceramic particles as shown in Figure 11. Rearrangement of all three phases (solid, liquid, and pores), caused by capillary-induced

viscous flow, will begin from the moment liquid is formed. In addition, dissolution and precipitation, pore growth and coalescence neck growth coarsening occur.

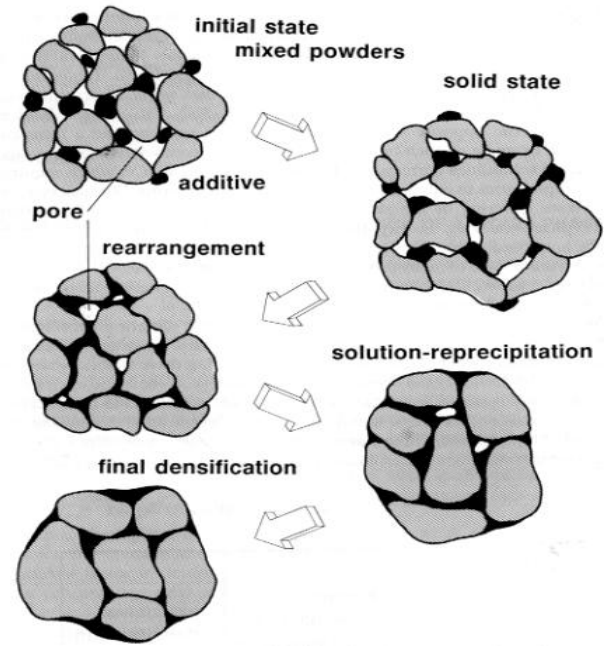

Figure 11. Stages involved in liquid phase sintering (Kim, 2004)

As an example, LPS is main mechanism at temperatures 900°C or higher in YSZ-Bi_2O_3 system because Bi_2O_3 melts at 825°C. The rate of densification has exponentially increased upon heating to around 1000°C (Kim, 2004). The densification of the powders is obtained from the capillary pressure of the liquid phase located between the ceramic particles. The requirements of the additive are high solubility of the ceramic in the liquid, appreciable wetting of the solid by the liquid and volume fraction under 25%. The major benefits of LPS are: (a) the enhanced densification rate and (b) the economic benefits arising from the use of a lower temperature than that required for direct sintering. A disadvantage of LPS is that the liquid phase used to promote sintering normally remains

as a glassy grain boundary phase that may lead to a deterioration of the properties at high temperatures.

The microstructure of YSZ is related to the sintering process; in particular, the sintering temperature at which densification of the powder occurs. It is generally known that as the sintering temperature of a material is reduced, the resulting grain size of the material becomes smaller and therefore a finer microstructure is produced. Two methods for reducing sintering temperatures of the YSZ are: (1) the use of ultra-fine powders and (2) the use of liquid phase sintering techniques.

Chapter 3. Experimental Work

The experimental work conducted in this study consists of acquisition of micro and nanoscale YSZ powders, preparation of powder compacts using a cold pressure die, sintering using laser shock waves, scanning electron microscopy (SEM) characterization and measurement of mechanical and thermal properties. Modeling work involved the prediction of the plastically affected depth, residual stress and plastic strain on the surface as a result of shock wave propagation. The study was aimed to provide a better understanding of the mechanisms of mechanical sintering of YSZ as a function of particle size. Due to its high ionic conductivity, LSP treated YSZ has many potential applications such as fuel cells and sensors.

3.1 Powder Acquisition

Cubic form of yttria-stabilized zirconia (c-YSZ) containing 8 mole% Y_2O_3 was selected for this research as the material because: 1) it is stable in the entire temperature range from room temperature to its solidus temperature of 2700°C; 2) it is readily available in different sizes from several sources; and 3) it has high ionic conductivity and high corrosion resistance useful for many applications such as sensors and solid oxide fuel cells.

Two different types of c-YSZ powders were procured from two vendors. The nanopowder was purchased from Inframat Advanced Materials Corporation; Nanox™ S4007 feedstock powder of YSZ (30-60 nm, 99.9% pure). This powder consists of agglomerated nanoparticles with high density and flowability. The crystallite size of nano-YSZ powder was 30-60 nm. However as described in Fig. 9, the composite grains

are clustered together forming agglomerates with a typical size range from 0.2 to 2 μm. For most part, agglomerates are smaller than 1 μm. The rationale for choosing nanopowders of c-YSZ are: 1) potential for very high oxygen conductivity due to the high oxygen diffusivity in the grain boundaries; 2) crack suppression during the sintering process due to its high ductility (Drings, Brossmann and Schaefer, 2007); 3) lower sintering temperature due to high surface area; 4) improved catalytic and sensoric properties due to their high surface area and minimal defects; and 5) increased fracture toughness and plasticity.

The micropowders of YSZ (202 NS, nominal size of 16 μm) were received from Sulzer Metco. Rare-earth oxide powders (Yb_2O_3 and Nd_2O_3) were obtained from Materials Preparation Center of Ames Laboratory located within Iowa State University. The purity of the rare-earth oxide powders is unknown. The purpose of the rare-earth oxide is to reduce thermal conductivity of c-YSZ through phonon-scattering.

3.2 Sample Preparation

These powders were used to make five different types of samples as listed in Table 3. The samples include micro YSZ, nano YSZ, and three different mixtures.

Table 3. List of samples with powder mixture

Sample	Powder Mixture
1 (MC)	Micro YSZ
2 (MOC)	5% Micro YSZ + 95% Rare-Earth O_2
3 (NC)	Nano YSZ
4 (50/50 MNC)	50% Micro YSZ + 50% Nano YSZ
5 (75/25 MNC)	75% Micro YSZ + 25% Nano YSZ

A Compac™ die press displayed in Figure 12a was used to compress the powders. The Compac™ press allows for maximum pressure of 172 MPa. This press is capable of using different sized dies. The die made of WC displayed in Figure 12b can withstand the maximum force of the press. Also, a wide range of powders can be used with this type of die. Operating procedures for the press and powder compaction are described in section 1.3 of the Appendix.

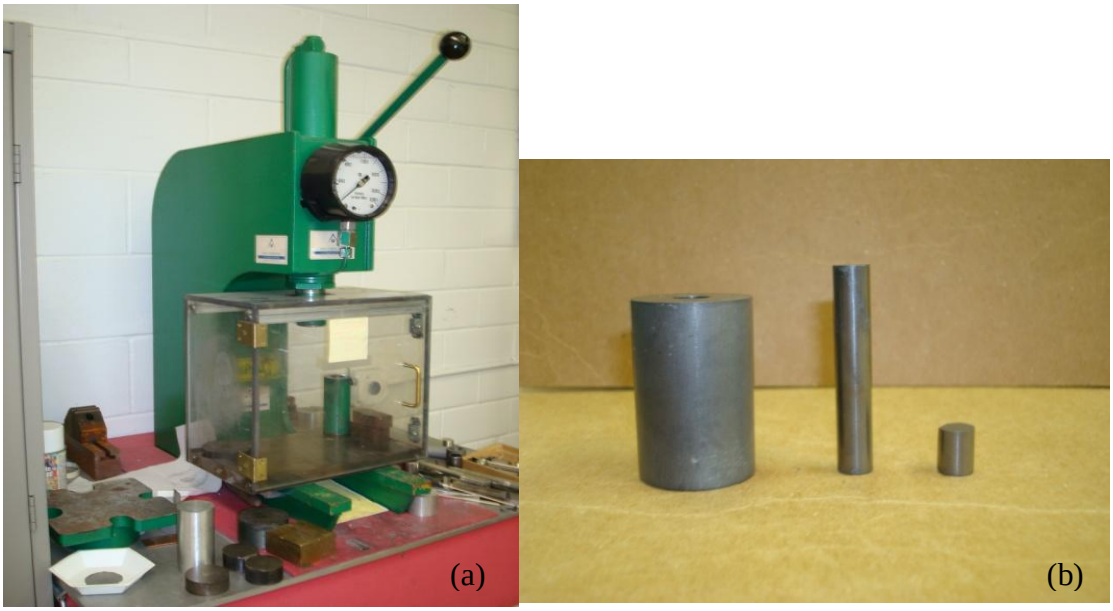

Figure 12. (a) Compac™ die press; (b) Tungsten carbide die

The powders were poured into the die and uniaxially cold-pressed by applying 69 MPa. After pressing, the compact was taken out from the die carefully and then the mass, diameter and thickness were measured and the bulk density was calculated (Table 4).

Table 4. Powder compact details

Sample	Powder Mixture	Trial	Weight (kg)	Thickness (m)	Diameter (m)	Volume (m^3)	Bulk Density (kg/m^3)
1	Micro YSZ	1	1.74E-04	1.13E-03	6.42E-03	3.65E-08	4.76E+03
1	Micro YSZ	2	1.57E-04	1.08E-03	6.44E-03	3.51E-08	4.49E+03
1	Micro YSZ	3	1.60E-04	1.09E-03	6.47E-03	3.59E-08	4.46E+03
2	95 % Micro YSZ + 5 % Rare-Earth O_2	1	2.41E-04	1.23E-03	8.05E-03	6.26E-08	3.85E+03
2	95 % Micro YSZ + 5 % Rare-Earth O_2	2	2.21E-04	1.25E-03	8.04E-03	6.33E-08	3.49E+03
2	95 % Micro YSZ + 5 % Rare-Earth O_2	3	2.18E-04	1.22E-03	8.05E-03	6.21E-08	3.50E+03
3	Nano YSZ	1	2.03E-04	1.16E-03	8.05E-03	5.91E-08	3.44E+03
3	Nano YSZ	2	2.09E-04	1.23E-03	8.06E-03	6.25E-08	3.34E+03
3	Nano YSZ	3	2.07E-04	1.21E-03	8.04E-03	6.15E-08	3.36E+03
4	50% Micro YSZ + 50% Nano YSZ	1	2.14E-04	1.24E-03	8.05E-03	6.31E-08	3.40E+03
4	50% Micro YSZ + 50% Nano YSZ	2	2.17E-04	1.17E-03	8.05E-03	5.95E-08	3.64E+03
4	50% Micro YSZ + 50% Nano YSZ	3	2.03E-04	1.05E-03	8.06E-03	5.33E-08	3.82E+03
5	75% Micro YSZ + 25% Nano YSZ	1	2.31E-04	1.24E-03	8.02E-03	6.27E-08	3.69E+03
5	75% Micro YSZ + 25% Nano YSZ	2	2.21E-04	1.26E-03	8.06E-03	6.41E-08	3.45E+03
5	75% Micro YSZ + 25% Nano YSZ	3	2.36E-04	1.23E-03	8.06E-03	6.27E-08	3.76E+03

Different observations and problems were noted during the cold pressing of the powders. The micro powders were the easiest powders to press. Most of the compacts were usable after being pressed with very few cracked samples. The larger particles bonded very well. The rare-earth oxides were mixed with the micropowders for a molar concentration of 95%. This powder mixture behaved similar to the micro powders. Both the micro and rare-earth compacts had a moderate surface finish with some rough edges.

The nano powders were the hardest to press. Very few samples were usable after being pressed since they tended to crack when removing them from the die. However, the samples that were usable had a very smooth surface finish with minor chipping on the

edges. A mixture of rare-earth oxide doped with nanopowders for a molar concentration of 5% was unsuccessful with the cold pressing. This powder mixture did not bond very well even with using different amounts of force. The samples had very rough surfaces, several chipped edges and cracks.

Two different mixture concentrations of micro and nano powders were used. These powder mixtures include: 50% micro and 50% nano molar concentration; 75% micro and 25% nano molar concentration. Both mixtures of the micro and nano powders behaved similarly. Cold pressing bonded the micro and nano powder mixtures very well. This was probably due to composite grains of the nano powders consisting of agglomerates which bonded with the micro particles. Both mixture showed minor chipping of the edges and had a similar surface finish to the micro compacts.

Since there is limited research conducted in LSP using ceramics, it was difficult to determine what type of wavelength, confining medium and ablative coating could be used. Currently many groups use a water confining medium. According to Figure 4, both glass and water confining-medium produce between 2 and 5 GPa of peak pressure. Molian's research group did a study on nanodiamond coatings yielding between 2.5 and 5 GPa of pressure in their experiment (Molian *et al*., 2009). Their results showed the highest microhardness value was from a water confining medium and a black paint coating. Also, it was shown that 532 nm and 1064 nm wavelength both provided satisfactory results.

3.3 Equipment for Laser Shock Peening

The equipment that was used for LSP process included a Nd:YAG laser and a xyz positioning table. A full detail of this equipment is listed below.

3.3.1 Quanta-Ray INDI Pulsed Nd:YAG Laser

The Quanta-Ray INDI Pulsed Nd:YAG Laser was chosen for this work. It is configured using a single rod and pump chamber. A high quality output beam is produced using a resonator design along with Quanta-Ray's unique gold-coated elliptical pump chamber. The thermal steady-state in the resonator is maintained by a constant flash lamp frequency, but the repetition rate of the light output can be varied.

The Q-switch mode allows the user to vary the repetition rate of the system between 1-10 Hz. The current laser setup allows for two different wavelengths which include 1064 nm and 532 nm. The 1064 nm wavelength has an average power (repetition rate) of 0.30 (1 Hz) - 1.66 Watts (10 Hz). The 532 nm wavelength has an average power (repetition rate) of 0.11 (1 Hz) – 0.40 Watts (10 Hz). The pulse duration of the laser is 5-7 ns. The peak power can reach as high as $2(10^7)$ Watts. The Quanta-Ray INDI Pulsed Nd:YAG Laser that was used in the experiment is displayed in Figure 13. Operating procedures for the laser can be found in section 1.1 of the Appendix.

Figure 13. Quanta-Ray INDI Pulsed Nd:YAG laser

3.3.2 Newmark Systems XYZ Positioning Table

Motion system is required for complete coverage of the sample surface because the focused beam size is very small compared to the sample size. Newmark system microslide linear stages are designed for space limited applications and can be configured in compact multi-axis assemblies. The stages offer very high resolution and smooth motion. They allow for a maximum load of 5 lbs while only weighing 1 lb. The stage can move up to 2 mm/sec and has a range of travel of up to 50 mm. The xyz table that was used is displayed in Figure 14. Operating procedures for the xyz table can be found in section 1.2 of the Appendix.

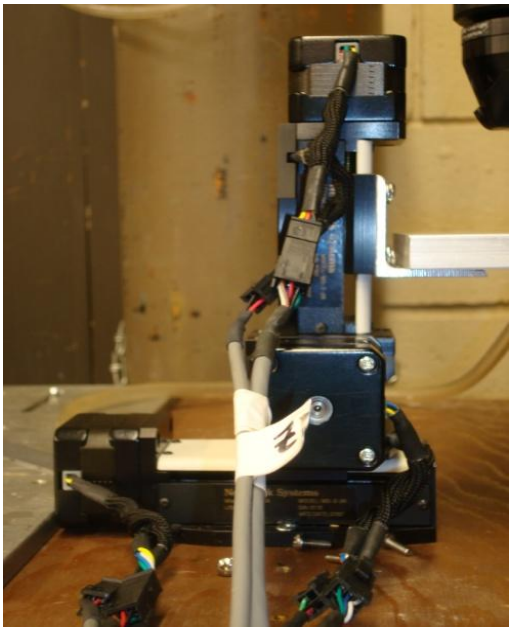

Figure 14. Newmark systems xyz positioning table

3.4 Experimental Setup

Figure 15 displays the experimental setup which includes the Quanta-Ray INDI Pulsed Nd:YAG Laser and the Newark XYZ table. Laser specifications are listed in Table 5. The setup includes the use of a custom made glass beaker. This beaker has an air valve that keeps the water from splashing on the lens during the experiment and a vertical stand where the sample can be placed. The beam guidance system consists of a 45° reflective mirror to reflect the beam downwards and a 6 mm plano convex lens to focus the beam. The focal length of the lens was 50 mm.

Table 5. Laser specifications (Wavelength = 532 nm)

Repetition Rate (Hz)	3	5	10
Power (W)	0.20-0.22	0.29-0.31	0.33-0.35

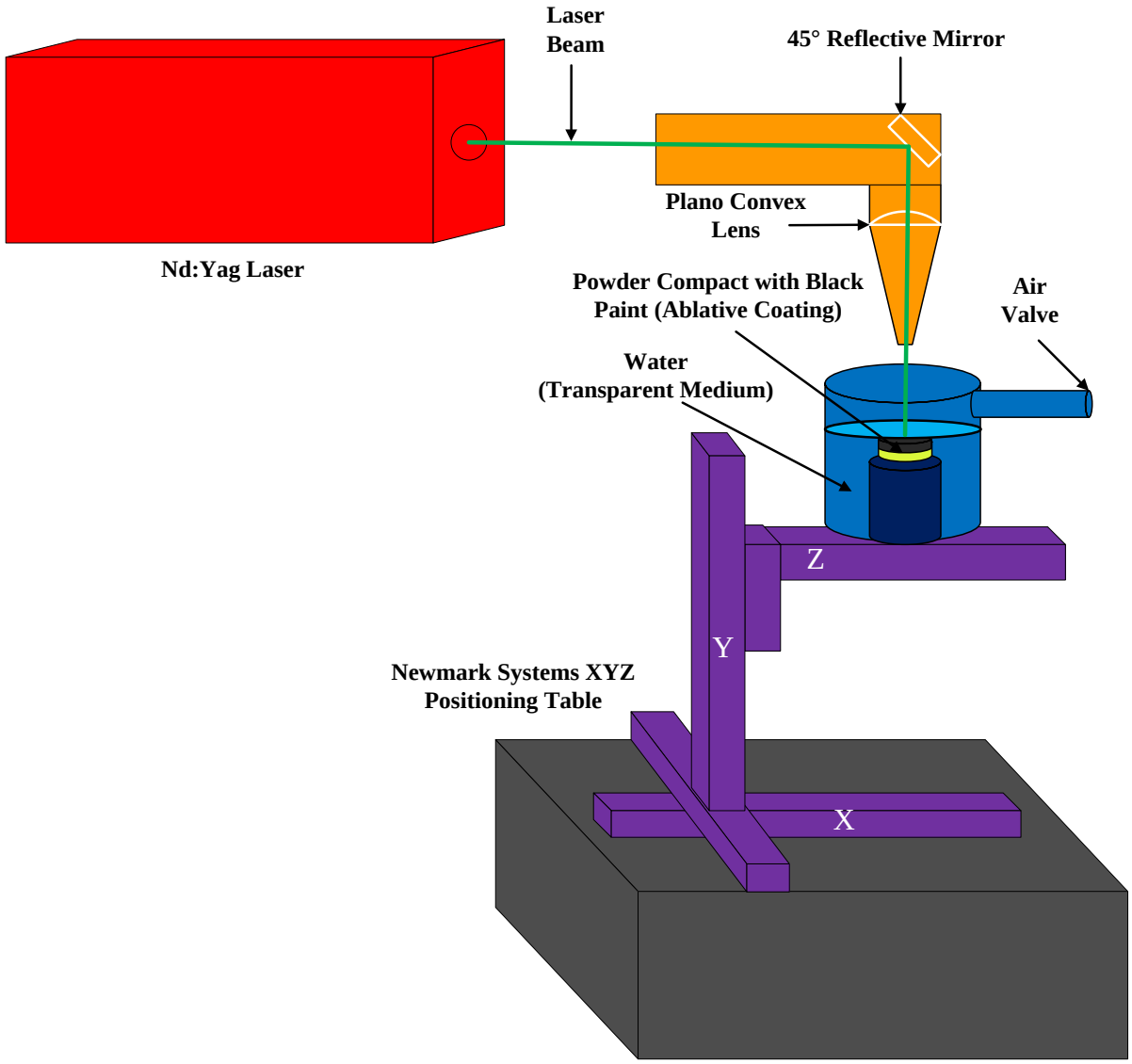

Figure 15. Experimental setup

3.4.1 Preliminary Calculations and Trials

The Nd:YAG laser can be set to two different types of wavelengths which are 532 nm and 1064 nm. Preliminary testing with the YSZ compacts using 532 nm at a high repetition rate caused the samples to break. It was determined that using 1064 nm would

be unsuccessful because the power generated at this wavelength was excessive. Using a 532 nm wavelength by frequency doubling limits the amount of power generated by the laser and could result in achieving the desired peak power density for the LSP process. The peak power density is calculated by using Equations 1 and 2 shown below. The research conducted by different groups referenced in Table 6 shows a range of 0.01-1000 GW/cm^2 for peak power density. However, the optimum range is between 1-100 GW/cm^2 to produce enough pressure in the target material.

Equation 1. Peak Power

$$\boldsymbol{Peak\ Power\ (W)} = \frac{\boldsymbol{Average\ Power\ (W)} \times \boldsymbol{Repetition\ Rate\ (s)}}{\boldsymbol{Pulse\ Width\ (s)}}$$

Equation 2. Peak Power Density

$$\boldsymbol{Peak\ Power\ Density\ (W/cm^2)} = \frac{\boldsymbol{Peak\ Power\ (W)}}{\boldsymbol{Area\ (cm^2)}}$$

Table 6. Peak power density used by different research groups

Variable	Units	Cheng, 2008	Molian, 2009	Montross, 2002	Caslaru, 2009
Average Power	Watts	3.93E-03	1.65	0.30	1.00
Repetition Rate	Seconds	0.20	0.33	0.10	0.03
Pulse Width	Seconds	1.00E-08	7.00E-09	1.00E-10	7.00E-09
Peak Power	Watts	7.85E+04	7.86E+07	3.00E+08	4.76E+06
Area	cm^2	7.85E-03	7.85E-03	7.85E-05	8.30E-06
Peak Power Density	GW/cm^2	*0.01	10.00	*1000.00	*574.02

*Calculated using values provided in references

The peak power density of the present system was then investigated. Different parameters of the laser would affect the peak power density. This includes the spot size of the beam and the repetition rate of the laser. The laser was set at 1 Hz which generated 70 mJ for the preliminary testing of various spot sizes. The beam was defocused at various lengths from the focal point in order to determine both quality and maximum peak power density of the spot sizes. These spot sizes were made on exposed x-ray film from one pulse of the laser and analyzed under the microscope to compare the damaged zone on the film to the theoretical spot size of the laser. The damaged zone on the x-ray film is displayed in Figure 16.

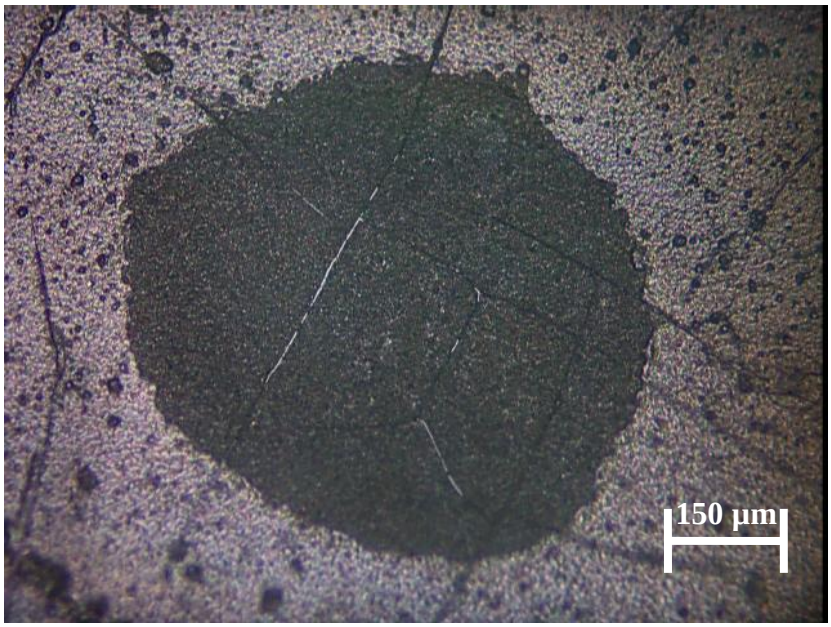

Figure 16. Damaged zone on x-ray film (9mm defocused length)

According to Gaussian beam propagation spot diameter (d_o) at focus is given by equation 3. This equation includes; M^2 which is *1/BP* where *BP* is the Beam Profile for a

near field fit (1m) of 0.70, λ is the wavelength of 532 nm, f is the focal length of 50 mm and D is the diameter of the lens of 6 mm.

Equation 3. Spot Diameter

$$d_o = \frac{M^2 4\lambda f}{\pi D}$$

The calculated spot diameter at focus is 8 µm which can be used in equation 4 and 5 to calculate the defocused spot size of the laser. Equations 4 and 5 include; z which is the defocused length, z_R is the Rayleigh length calculated using equation 5, λ is the wavelength of 532 nm and w_o is the beam waist which is $d_o/2$.

Equation 4. Defocused Spot Size

$$d(z) = d_o \sqrt{1 + \left(\frac{z}{z_R}\right)^2}$$

Equation 5. Rayleigh Length

$$z_R = \frac{\pi {w_o}^2}{\lambda}$$

Investigation of the damaged zones and theoretical spot size calculations at various defocused lengths is displayed in Table 7. It was concluded to use a defocused length of 9 mm because it produced the best quality on the x-ray film, the highest peak power density, and it was closely matched to the theoretical spot size calculations.

Table 7. Spot size specifications on x-ray film

Defocused Length (mm)	Damaged Zone Spot Size (mm)	Calculated Spot Size (mm)
9	0.64	0.76
14	0.95	1.18
19	1.45	1.60
24	not round	2.02

Different absorptive coatings and transparent overlays were attempted. Preliminary testing proved to be unsuccessful in some cases as seen in Table 8. This occurred when the laser was not able to generate enough power to vaporize the coatings off the YSZ compacts. This was seen when using a glass or water confining medium with both aluminum foil and black tape coatings. Using the black paint for both mediums was successful, but with some concerns. The glass confining medium resulted in black paint residue on the bottom of the glass. The water confining medium resulted with the water being contaminated with the black paint residue. Both of these concerns could be resolved with replacing the glass or water after every trial. However, the previous research conducted on the nanodiamond powders showed almost twice the value in hardness with using a water confining medium at 532 nm wavelength (Molian *et al*., 2009). After carefully analyzing the results of the preliminary testing, it was decided that using a water confining medium and a black paint coating would be the best choice.

Table 8. Preliminary testing on confining mediums and ablative coatings

Confining Medium	Ablative Coating	Results
Glass	Aluminum foil	Unsuccessful
Glass	Black Tape	Unsuccessful
Glass	Black Paint	Successful
Water	Aluminum foil	Unsuccessful
Water	Black Tape	Unsuccessful
Water	Black Paint	Successful

The repetition rate could now be analyzed for the laser. Preliminary testing of the samples showed different results with various repetition rates as seen in Table 9. Both 3 and 5 Hz were able to completely remove the black paint from the samples without breaking the YSZ compacts.

Table 9. Preliminary testing on repetition rates

Repetition Rate (Hz)	Results
1	Paint not fully removed
3	Paint removed
5	Paint removed
7	Sample broken
10	Sample broken

Preliminary testing concluded with using a set of criteria as follows; water confining medium, black paint coating, 0.76 mm spot size and two repetition rates. The theoretical spot size was used since the x-ray film is not an accurate measurement due to the thermal diffusion of the film. The peak power densities of the experiment were calculated and listed in Table 10. Using Figure 6, the maximum pressure corresponding to the peak power densities was estimated to be approximately 2.9 GPa for 5 Hz and 3.1 GPa for 3 Hz.

Table 10. Peak power densities of the experiment

Variable	Units	5 Hz	3 Hz
Average Power	W	0.30	0.21
Repetition Rate	Sec	0.20	0.33
Pulse Width	Sec	7.00E-09	7.00E-09
Peak Power	W	8.57E+06	1.00E+07
Area	cm^2	4.54E-03	4.54E-03
Peak Power Density	GW/cm^2	1.89	2.20

3.4.2 LSP Experiments

The experimental trial consisted of three samples for each type of powder composition. All the samples were coated with black paint. Two types of black paints were used which include: ultra-flat and flat. The samples had a much smoother surface finish when using the ultra-flat black paint. Using either repetition rate removes both types of paints from the samples. Also, the samples were placed 2 mm below the surface of the water. A list of all the samples and laser parameters of the experiment can be seen in Table 11.

Table 11. Experimental Details

Sample	Powder Mixture	Trial	Rep. Rate (Hz)	Avg. Pwr. (W)
1	Micro YSZ	1	3	0.21
1	Micro YSZ	2	5	0.3
1	Micro YSZ	3	5	0.3
2	95 % Micro YSZ + 5 % Rare-Earth O_2	1	3	0.21
2	95 % Micro YSZ + 5 % Rare-Earth O_2	2	5	0.3
2	95 % Micro YSZ + 5 % Rare-Earth O_2	3	5	0.3
3	Nano YSZ	1	3	0.21
3	Nano YSZ	2	5	0.3
3	Nano YSZ	3	5	0.3
4	50% Micro YSZ + 50% Nano YSZ	1	3	0.21
4	50% Micro YSZ + 50% Nano YSZ	2	5	0.3
4	50% Micro YSZ + 50% Nano YSZ	3	5	0.3
5	75% Micro YSZ + 25% Nano YSZ	1	3	0.21
5	75% Micro YSZ + 25% Nano YSZ	2	5	0.3
5	75% Micro YSZ + 25% Nano YSZ	3	5	0.3

Experimental procedures can be found in section 2 of the Appendix. Since the laser was set to two different repetition rates, different speeds on the xy table were used to account for this. The xy table was set to a speed of 0.15 mm/s for 3 Hz and 0.5 mm/s for 5 Hz. Using these speeds resulted in overlap between pulses therefore causing multiple LSP. The calculated overlap using the theoretical spot size for 3Hz is 0.71 mm and for 5 Hz is 0.66 mm. The command script used in the experiment can be seen in section 3 of the Appendix. The program was set to follow the path shown in Figure 17. The beam was set on the edge of the sample before each trial run and was programmed to only cover half of the sample. This allowed for testing on both treated and untreated sides.

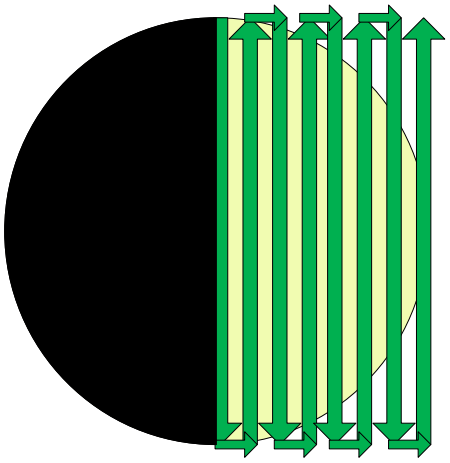

Figure 17. Programmed beam path

3.5 Scanning Electron Microscopy Analysis

The Scanning Electron Microscope (SEM) is a microscope that uses electrons rather than light to form an image. The SEM has a large depth of field, which allows a

large amount of the sample to be in focus at one time. Also, it produces images of high resolution, which means that closely spaced features can be examined at a high magnification. Samples must be conductive in order for the image to be displayed. The Scancoat Six SEM Sputter Coater was used to deposit a thin gold film on the samples. Approximately 50-100 nm of gold was sputtered at 5 mbar. The JEOL JSM-6060LV Low Vacuum Scanning Electron Microscope was used for the imaging of the samples. The SEM was set with a parameter of 20 kV.

3.5.1 Scancoat Six SEM Sputter Coater

The Scancoat Six is a compact sputter coater designed to prepare specimens for conventional scanning electron microscopy (SEM). It allows a wide variety of specimens to be coated with a high quality, conductive metal film. Gold films are deposited uniformly, even over re-entrant surfaces. The sputter coater is displayed in Figure 18. Operating procedures for the sputter coater can be found in section 1.5 of the Appendix.

Figure 18. Scancoat Six sputter coater

3.5.2 JEOL JSM-6060LV Low Vacuum Scanning Electron Microscope

The JSM-6060LV is a high-performance scanning electron microscope (SEM) with capability for secondary electron imaging and backscattered electron imaging. The specimen chamber can accommodate a specimen of up to 5 inches in diameter. The low vacuum (variable pressure) mode allows for samples that cannot be viewed at high vacuum because of a nonconductive surfaces or excessive water content. It has an accelerating voltage parameter of 0.5 to 30.0 kV and a magnification range of x5 to 300,000. The Scanning Electron Microscope that was used is displayed in Figure 19.

Figure 19. JEOL JSM-6060LV low vacuum scanning electron microscope

3.6 Microhardness Measurements

Microindentation hardness testing is a microscopic scale technique used to measure the hardness of a material. A few grams to 1 kg of force are applied through a precision diamond probe to the surface of the material. The impression length and the test load are used to calculate a hardness value. This hardness value is useful to determine a material's properties and expected service behavior. The Wilson Tukon Hardness Tester was used to test the microhardness of each type of sample both treated and untreated surfaces. A force of 1 kg_f was applied to the surface of these samples.

3.6.1 Wilson Tukon Hardness Tester

The Wilson Tukon Hardness Tester was used to produce microindentations on the surface of the YSZ compacts to measure the hardness. This instrument contains a modular turret design for varying configurations of objectives and indenters. It has a test force range of 10 g_f – 1 kg_f. The hardness tester is displayed in Figure 20. Operating procedures for the hardness tester can be found in section 1.4 of the Appendix.

Figure 20. Wilson Tukon hardness tester

3.7 Thermal Conductivity Measurements

Thermal conductivity of powder compacts was measured using a Transient Electro Thermal (TET) technique described in (Guo, Wang and Wang, 2007). The scheme of the TET technique is shown in Figure 21. Thin long samples were carefully prepared and displayed in Figures 22-25. The samples that were measured include MC 1-3, NC 1-3, 50/50 MNC 4-1 and 75/25 MNC 5-1. TET technique enables the measurement of thermal diffusivity. Thermal conductivity is then calculated upon knowing the density and specific heat of YSZ. The density of the samples after sintering was measured as 2650 kg/m^3 which is near the full density of 2700 kg/m^3. The specific heat is assumed as 547 J/kg K (Pinto *et al*., 2006).

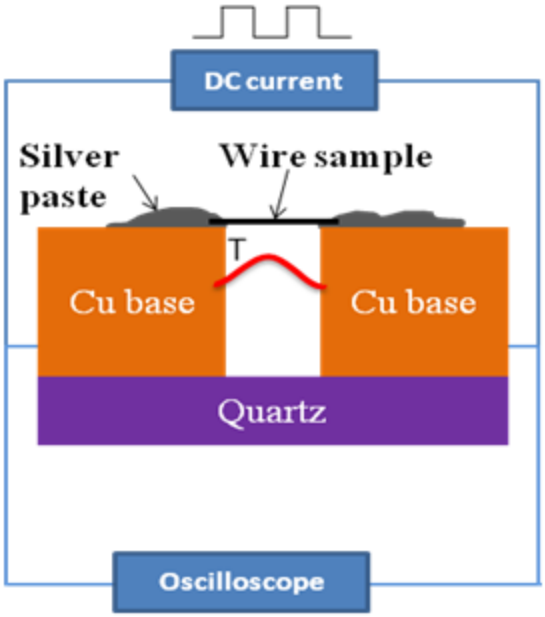

Figure 21. Schematic of TET method (Guo, Wang and Wang, 2007)

The sample is suspended between two copper electrodes and the two ends are glued with silver paste to reduce both thermal and electrical contact resistance. Also, the sample is put into a vacuum chamber with the pressure below 1×10^{-3} torr to make the heat convection negligible. Electrical heating through the sample is induced by applying a constant DC current. The heating causes temperature evolution of the sample which is tightly related to the heat transfer along the sample. If the sample has a linear correlation (positive or negative) between electrical resistance and temperature in a certain temperature range, the temperature evolution of the sample can be sensed by measuring the voltage evolution when the current is constant. Periodical electrical heating is applied with a square wave of DC current for the convenience of experiment parameters changes, such as electrical current and recording time. During this process, simultaneous time

period recordings of the same experiment can be done to allow for repeatability. It should be mentioned that this time period of the square wave current should be chosen carefully because of the heat transfer process. The heat transfer process must reach steady state and return to its initial state during the time period of the square wave. Because of this transient process, the current source of the device should have a very small rising time compared to the time it takes to reach steady state.

In this experiment, the Model 6221 AC and DC current source with 2 μs rising time from Keithley Instrument Inc. is used. The voltage evolution is monitored and recorded by Tektronix TDS7054 Digital Phosphor Oscilloscope which has the maximum sample rate 5 GS/s. Consequently, the thermal diffusivity of the sample can be obtained by fitting the normalized temperature evolution curve against time with a robust program.

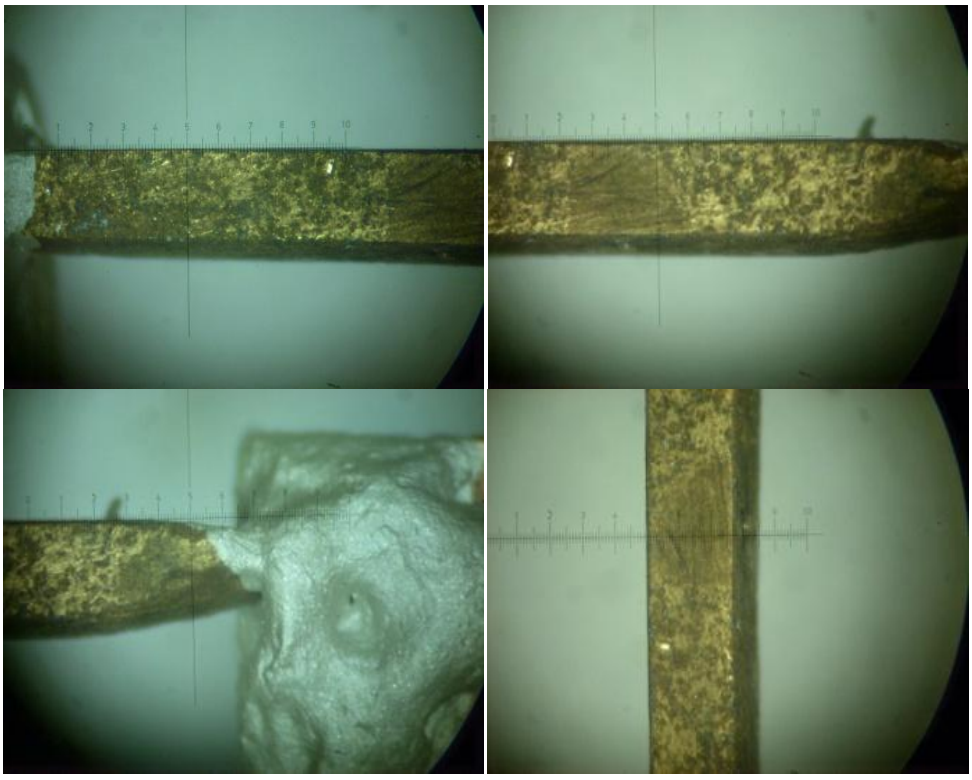

Figure 22. Test sample MC 1-3 for TET technique

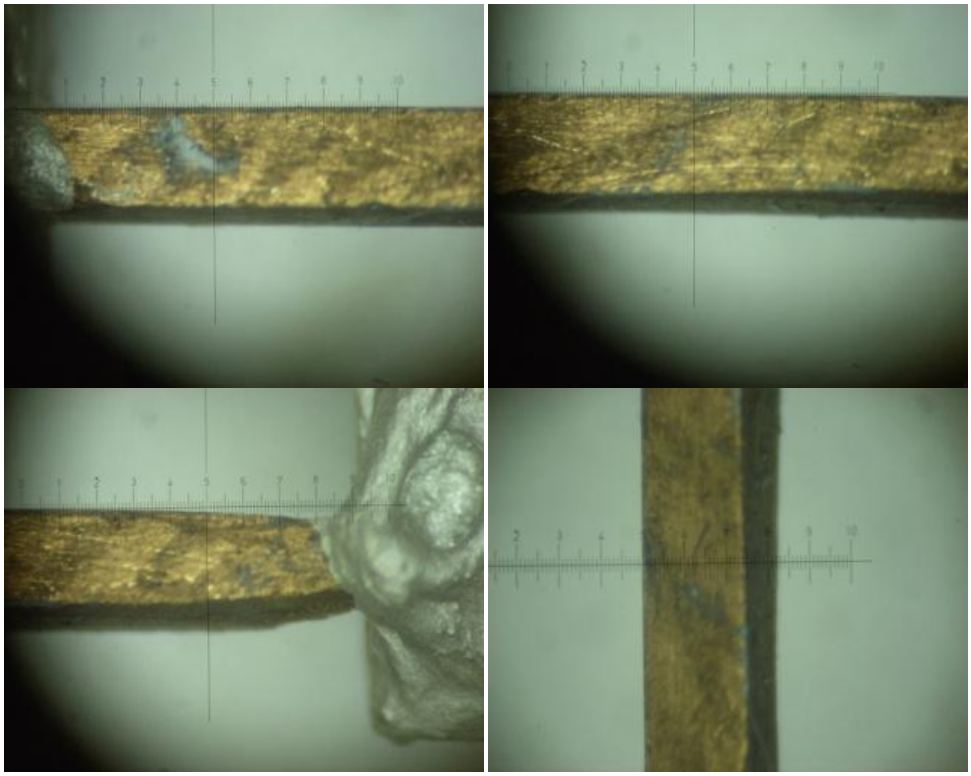

Figure 23. Test sample NC 3-3 for TET technique

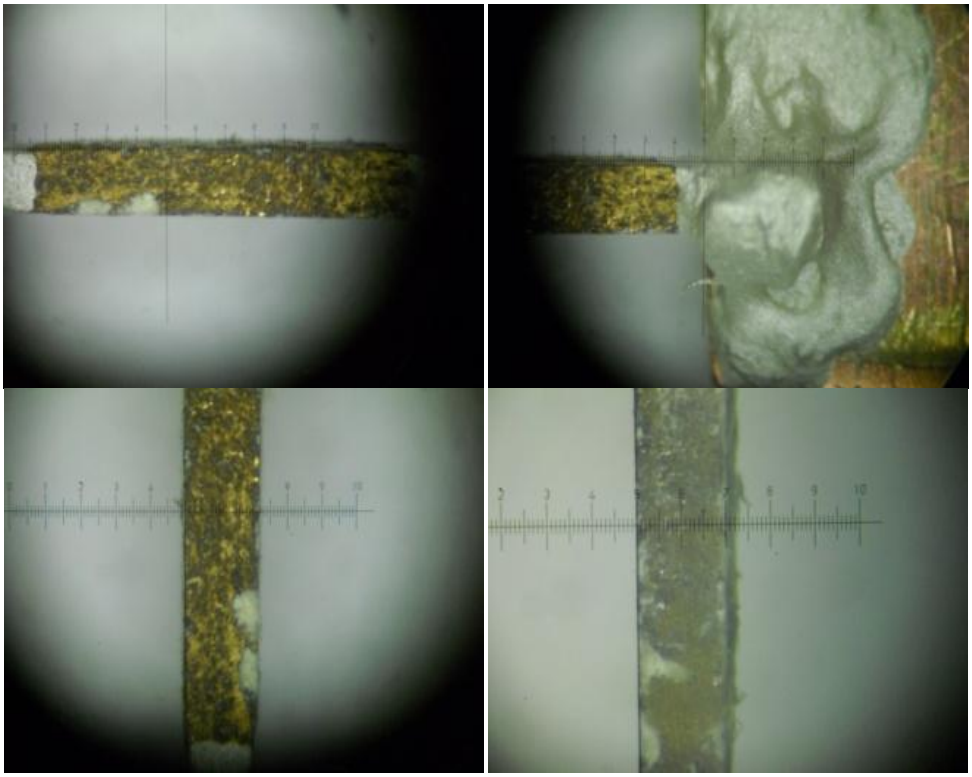

Figure 24. Test sample 50/50 MNC 5-3 for TET technique

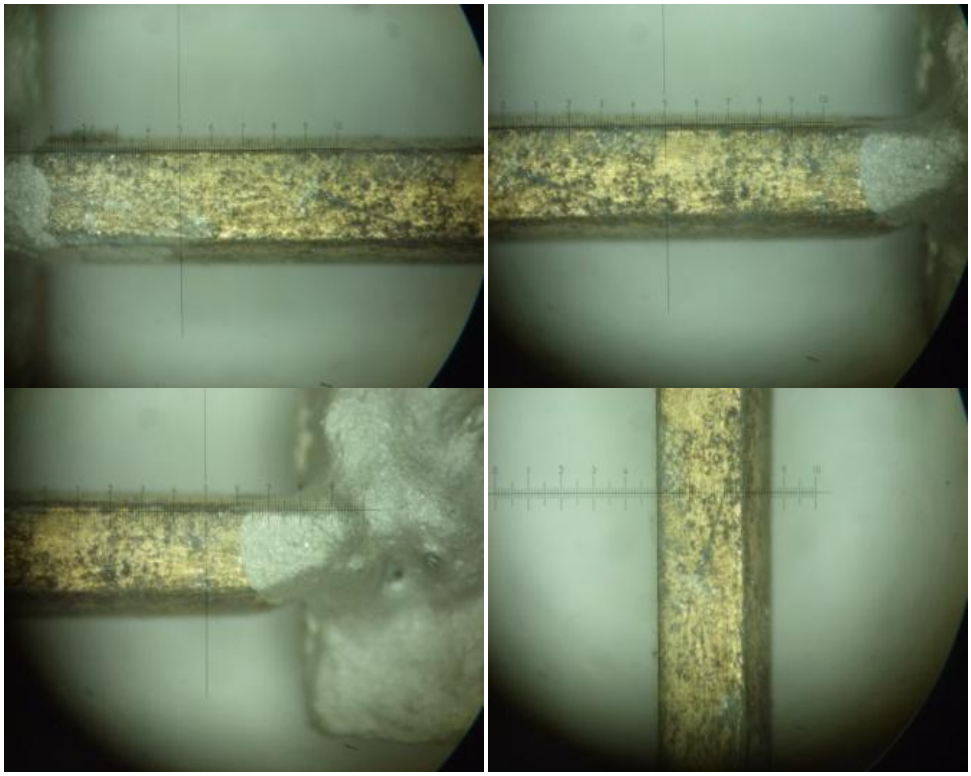

Figure 25. Test sample 75/25 MNC 5-3 for TET technique

Chapter 4. Results and Discussion

Experiments yielded successful results as described below. The black paint was fully removed from the surface of the samples and the plasma was visible during the LSP process. The process took less than a few minutes for each sample. After conducting all the trials a few generated observations were noted. When using 3 Hz, chipping or cracking was seen on most of the samples. Most of the compacts that used 5 Hz turned out well. However, severe cracking was seen on the MC samples with both repetition rates, while most of the MOC samples were very smooth. The rare earth oxide and the diameter were the only differences between the MC and MOC samples. These samples should have displayed similar results, but this was not the case. Most of the NC samples were also very smooth.

4.1 Scanning Electron Microscopy Results

SEM is an excellent tool for revealing the details of the effects induced by LSP. Hence, the quality of LSP samples was examined in SEM with specific attention to porosity, cracking and chipping. SEM was conducted on samples from trial 1 of MC, NC and 50/50 MNC.

Figure 26 shows SEM micrographs of three powder compact samples. It may be noted that only half of the sample area was subjected to LSP for comparison with the untreated surface. In the MC sample, excessive cracking and chipping on the surface can be seen. The stresses induced by LSP have exceeded fracture strength of YSZ leading to “bursting” and subsequent formation of a network of cracks. The overlapping laser scans may be noted in Fig. 26a. Cracks appear randomly and the material has fragmented. As

shown in the experimental stress distribution plot of LSP in Fig. 8, there is a tensile stress outside the laser spot region giving rise to the possibility for crack formation. In contrast, the NC and MNC samples did neither reveal the presence of any cracks nor any major edge chipping. However the surface profile appeared much rougher particularly with the NC sample (Fig. 26b).

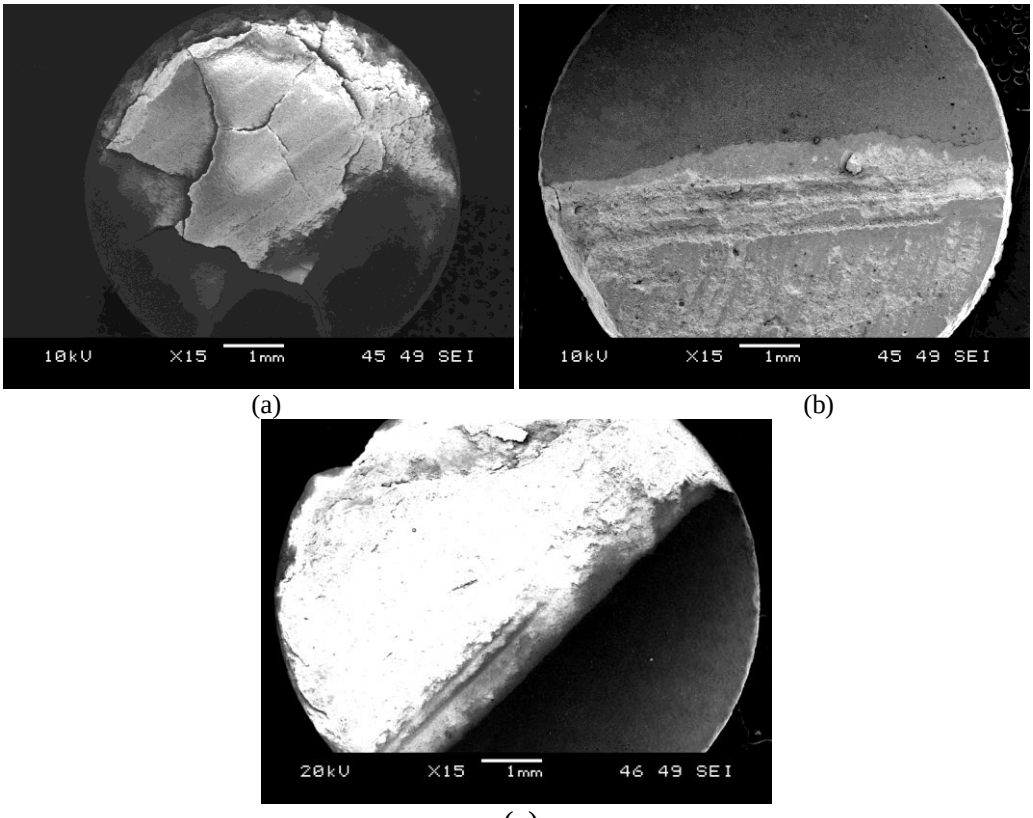

(a) (b)

(c)

Figure 26. Laser shock wave sintered YSZ powder compacts: (a) MC 1-1; (b) NC 3-1; (c) 50/50 MNC 4-1

Figure 27 shows the SEM micrographs of untreated and LSP treated MC both at low and high magnifications. The untreated surface already contains some fine cracks

(Fig. 27a) that might have been nucleated for the larger cracks seen in the LSP sample. Higher magnification micrographs reveal the densification and finer grain size in LSP samples. Thus SEM analysis of the MC sample indicates that the pre-cracks from the cold pressing operation coupled with lack of ductility of micro-sized powders account for the development of large network of cracks during LSP.

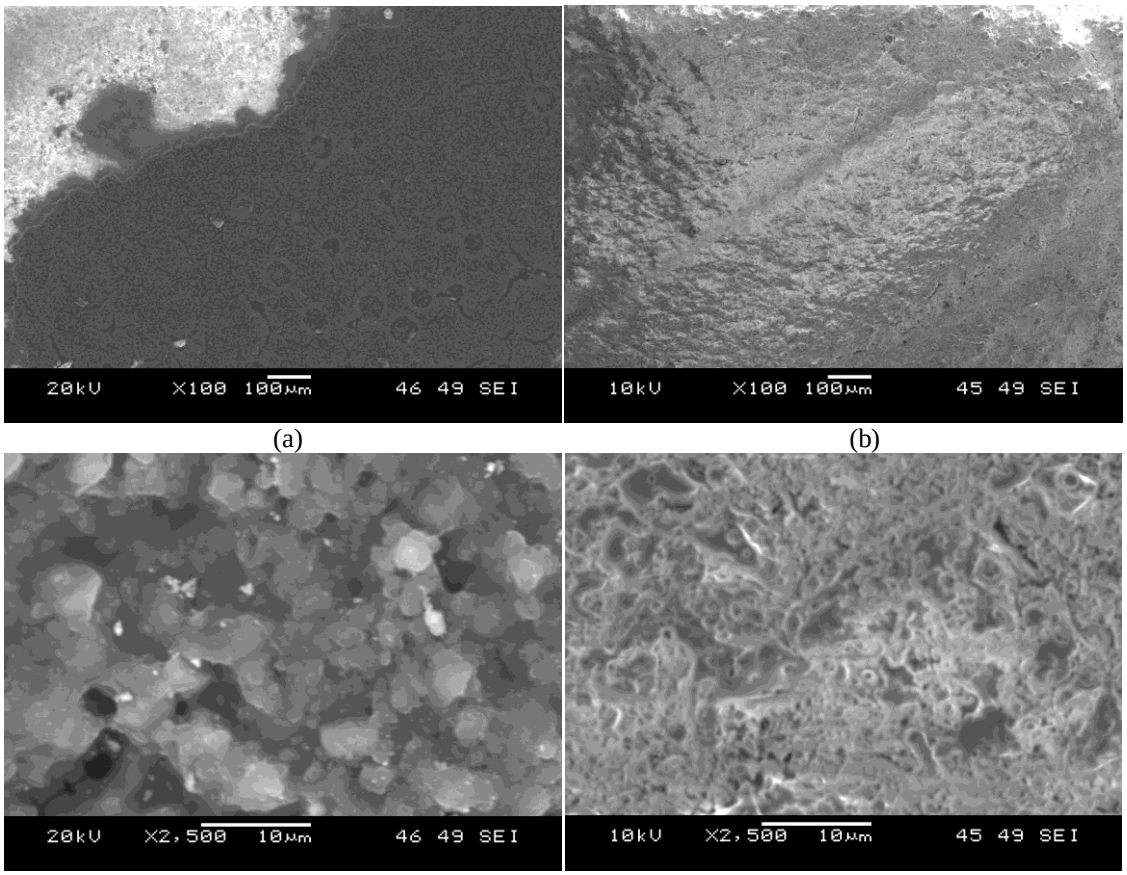

Figure 27. MC 1-1 (a, c) Untreated (b, d) LSP treated regions without cracks

SEM micrographs in Figure 28 display a comparison between untreated and LSP treated NC at both low and high magnifications. Powder compact prior to LSP was smooth with no evidence of any fine cracks (Fig. 28a) unlike the MC sample. However LSP created a disturbed surface with some material apparently ablated. It appears that

stresses developed in LSP also caused material removal from the surface while consolidating the bulk. Although higher magnification micrographs reveal the densification effect, there is an apparent coarsening of grains compared to the MC sample. Another intriguing feature is the area above the first pass where the paint was removed from the plasma created on the first pass (Fig. 29a-b). Figure 29c displays finer grain structures compared to the untreated area in Figure 28c. It seems when an area is exposed to plasma without direct contact from the beam, a grain refinement effect occurs. In the subsequent passes, there is clear evidence of localized material removal caused either due to the loose nanopowders or by the stress-assisted removal of particles.

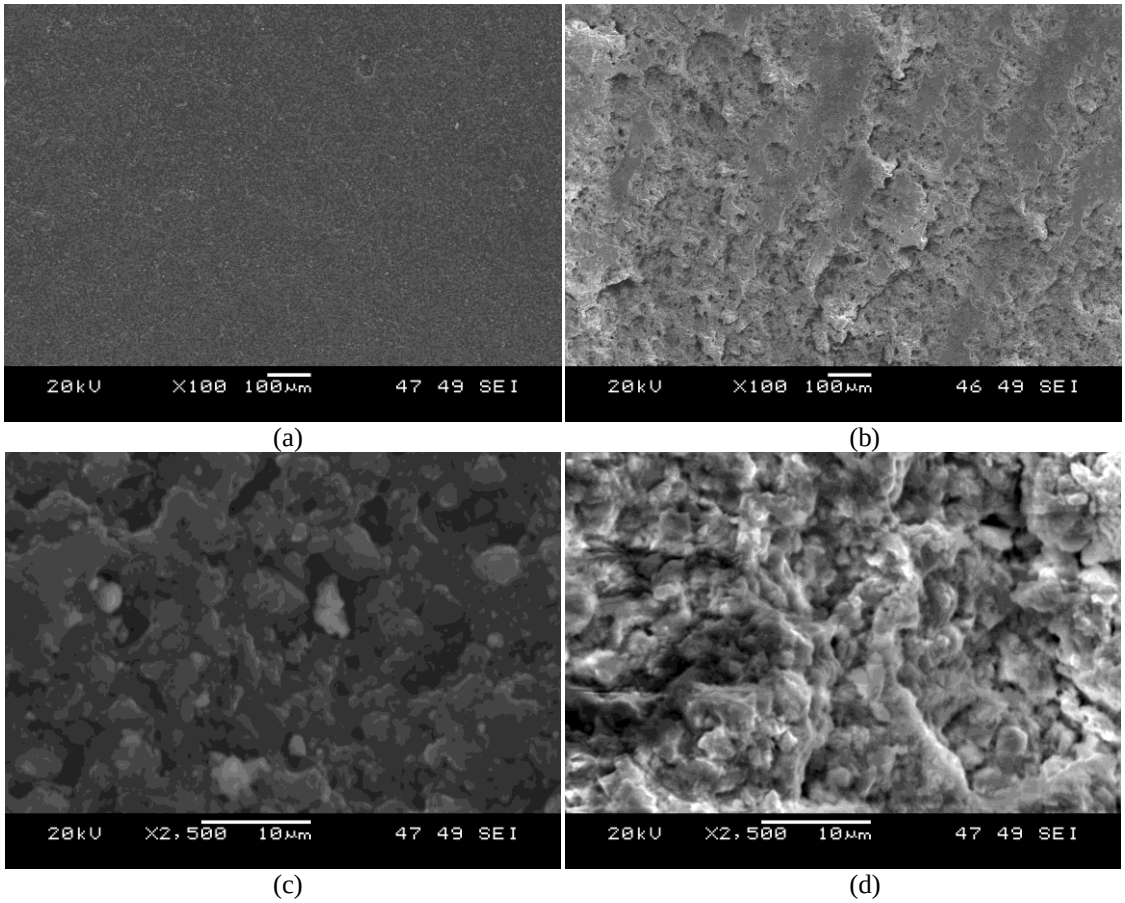

Figure 28. NC 3-1 (a, c) Untreated (b, d) LSP treated regions

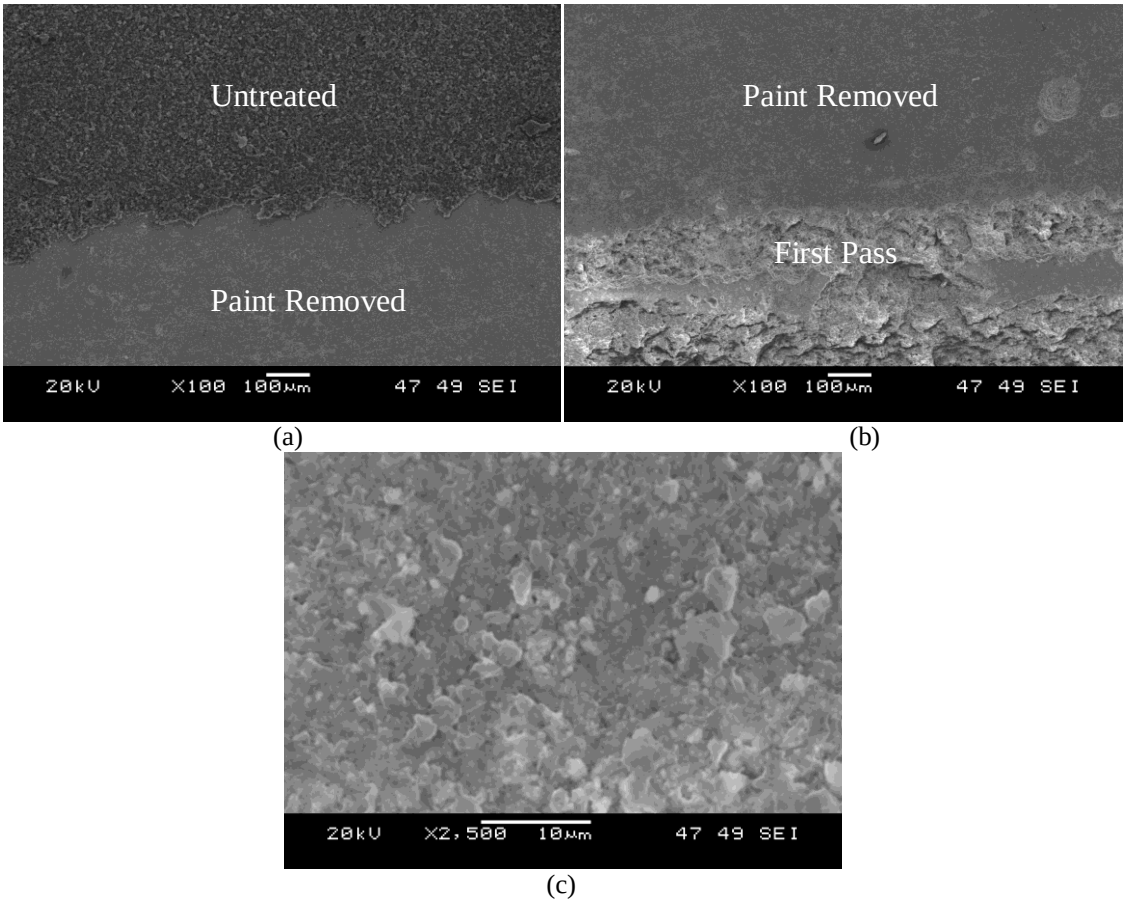

Figure 29. NC 3-1 (a) Untreated/Paint Removed; (b) Paint Removed/First pass in LSP; (c) Paint Removed Area

Figure 30 shows the SEM micrographs of 50/50 MNC with attributes intermediate to those of MC and NC. There are no visible cracks on either untreated or LSP treated regions. Also, there is no ablation like the MC but then there is grain coarsening similar to that the NC sample.

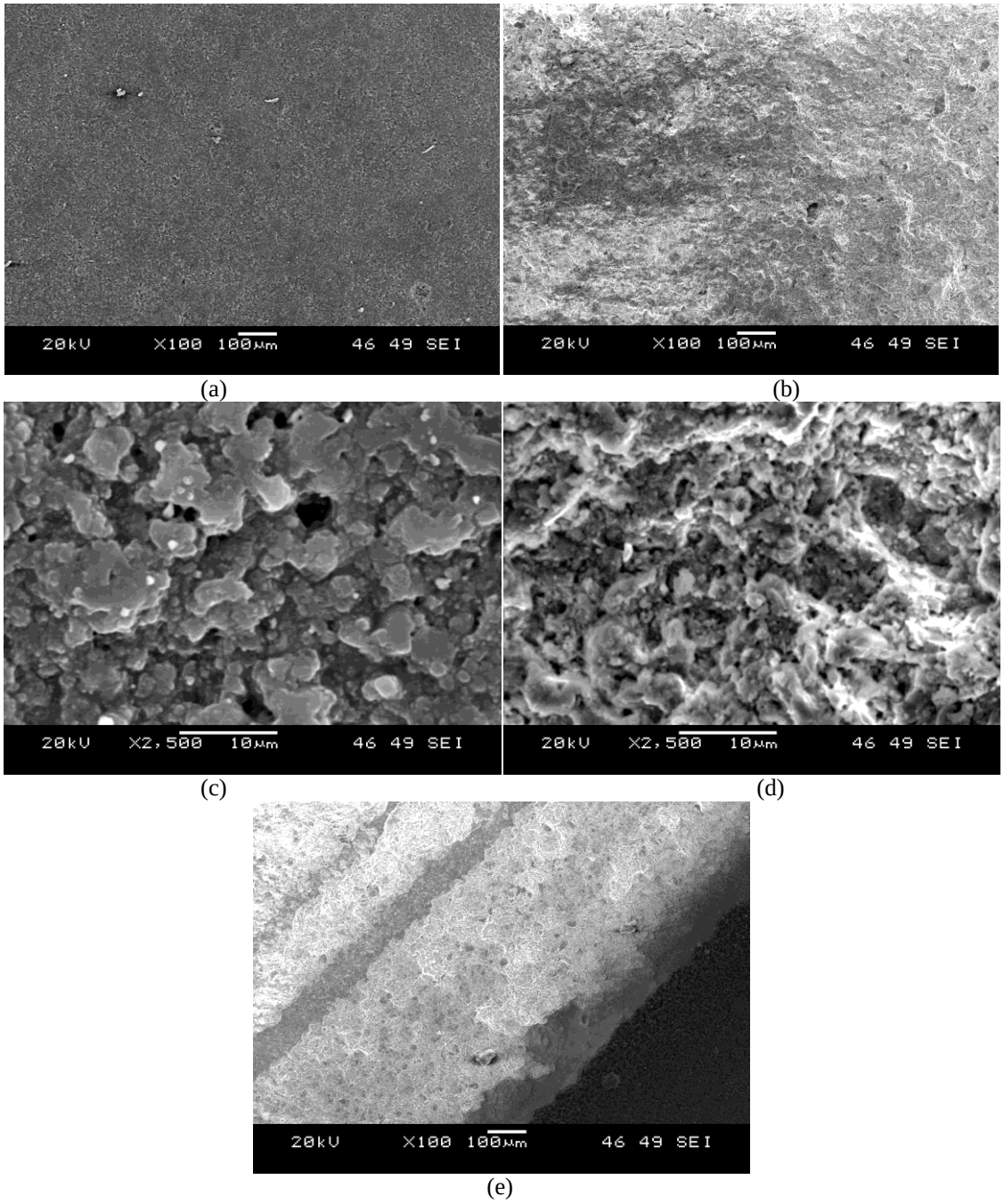

Figure 30. 50/50 MNC 4-1 (a, c) Untreated (b, d, e) LSP treated regions;

Based on the SEM analysis, it may be concluded that LSP generated cracks in the micropowders and ablation in the nanopowders. In addition, there is inhomogeneous sintering and more grain coarsening in nanopowders as opposed to micropowders.

Because of their small size, nanopowders are susceptible to form agglomerates and the compaction of such agglomerated powders tends to cause an inhomogeneous density distribution within a green body. Furthermore the total frictional resistance offered by the large number of particle-particle point contacts per unit volume leads to the inhomogeneous compaction.

In regards to grain coarsening with nano YSZ, two different mechanisms, proposed by Nakaso's research group, may be contemplated (Nakaso, Shimada, Okuyama and Deppert, 2002). Both mechanisms depend on the strength of the bonds between the particles as shown in Figure 31. With strong bonds which is usually the case with nanopowders, coalescence is the main mechanism and the primary particles subsequently fuse together to form a compact particle.

The second mechanism is rearrangement of crystallites where the bond strength between the crystallites could be weak. Nanoparticles enhance coarsening of YSZ crystallites due to increased surface mobility. The small size of grains in nanopowders provides a strong capillary driving force to reduce the total surface and interfacial energies of the system. This driving force can be dissipated either by coarsening of crystallites (without much densification) or by the elimination of pores (i.e., densification).

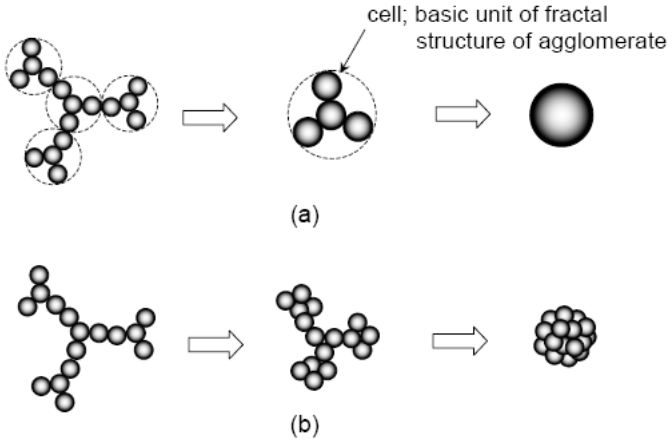

Figure 31. Schematic illustration of the change of particle morphology during sintering process: (a) Sintering model 1: surface area change; (b) Sintering model 2: rearrangement of primary particles (Nakaso *et al*., 2002)

Densification in nano YSZ is better than in micro YSZ due to the presence of large stresses that may cause a phase transition in nano YSZ. For example, a recent study in low temperature thermal sintering of nano YSZ revealed the formation of monoclinic phase at the grain boundaries; this was attributed to the presence of stresses (Kim, 2004). In addition, stresses assisted in particle rearrangement which is the rotation and sliding of particles leading to some densification (Kim, 2004). Thus, we hypothesize that in our study, shock waves create a compressive stress pattern that causes plastic deformation of the nano particles and a large increase in the concentration of vacancies on the surface of the particles; this highly defective surface coupled with a high surface mobility of nanoparticles is responsible for the mass transport. In addition the strong bonding between nanoparticles and stress-assisted formation of monoclinic phase at the grain boundaries reduce significantly the pores thus resulting in a high density part.

4.2 Microhardness Testing Results

Results of the microhardness testing are displayed in Figures 32-34. The average microhardness values are shown in Table 12. Three measurements were taken for each sample on both the treated and untreated sides. Microhardness testing was done on all five samples from trial 2. A distance of 100, 200 and 300 µm from the center was varied to determine the extent of the LSP process. The increase in hardness was very uniform throughout the samples. Surprisingly, the average Vickers hardness of the samples on the untreated surface resulted with very close values with a range of 216-235 Kg_f/mm^2. The treated surfaces of the samples had a larger range of 311-386 Kg_f/mm^2. The MOC and MC had the largest increase in Vickers hardness with a value of 64%. A trend of increasing hardness dependent on the powder composition can be seen. The samples containing the larger nano powder composition resulted with less increase in hardness.

Table 12. Results of microhardness testing

Sample	Avg. HV (Kg_f/mm^2)	HV % Increase
Treated MC	381	64
Untreated MC	232	
Treated MOC	386	64
Untreated MOC	235	
Treated NC	311	44
Untreated NC	216	
Treated 50/50 MNC	333	54
Untreated 50/50 MNC	217	
Treated 75/25 MNC	354	62
Untreated 75/25 MNC	219	

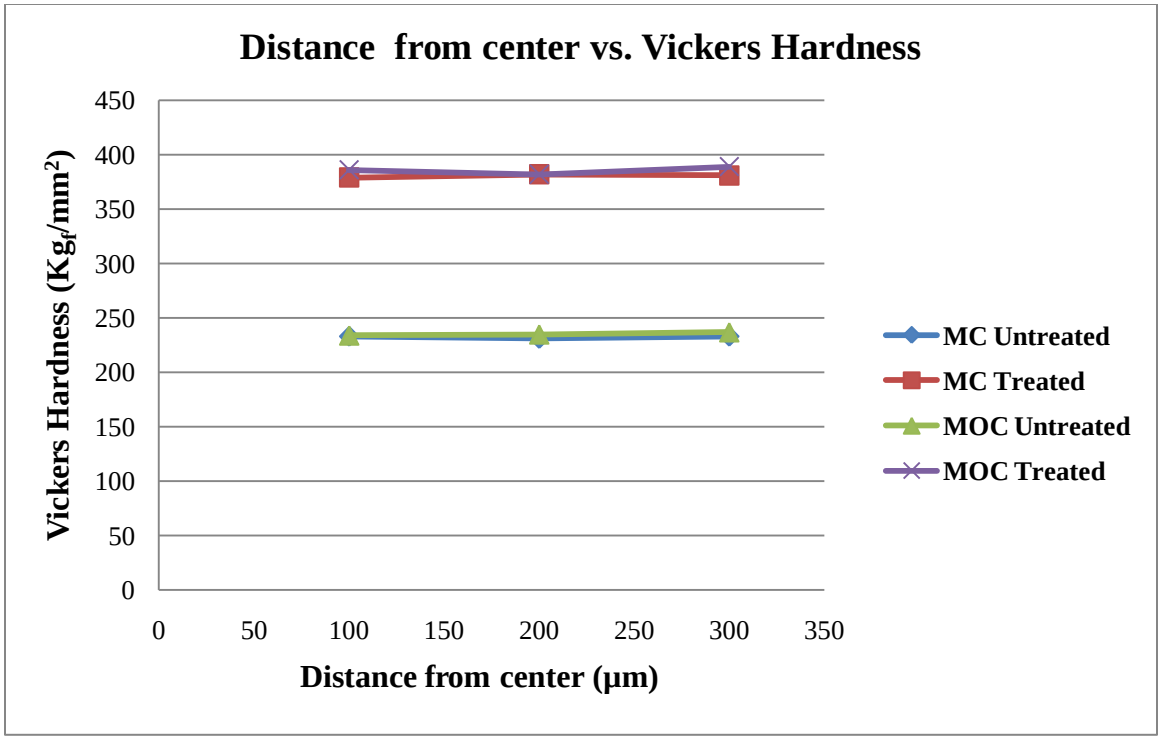

Figure 32. Microhardness testing results for MC and MOC samples

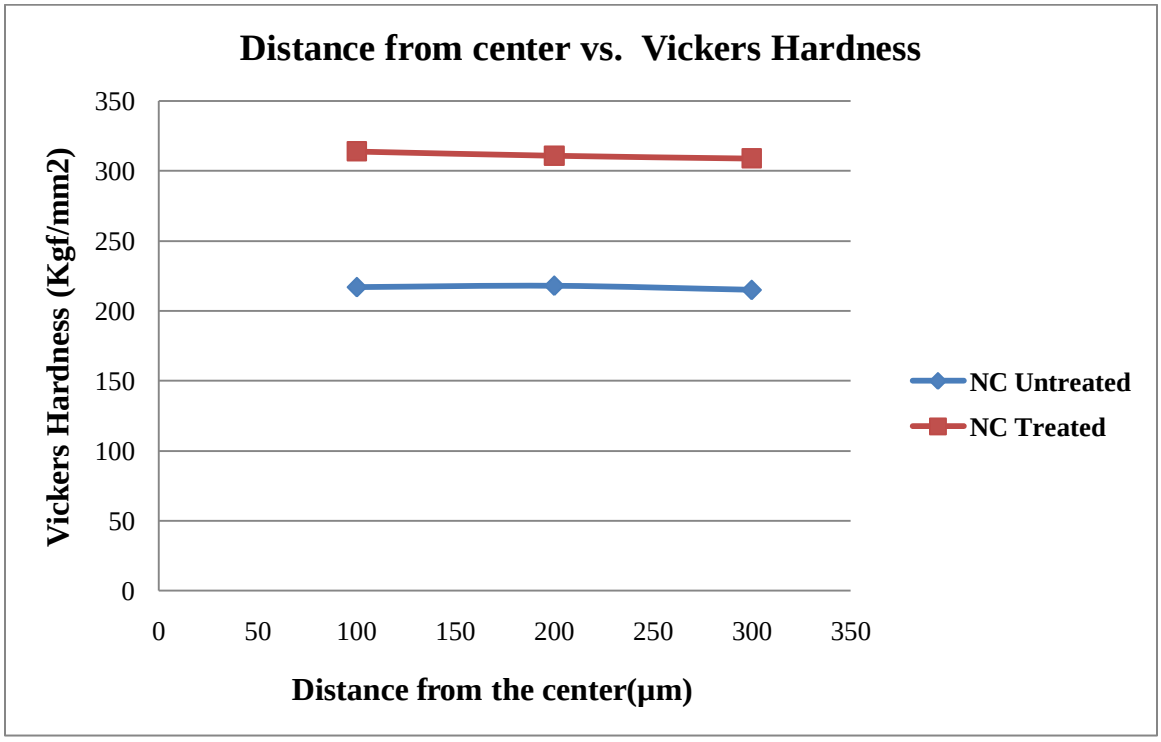

Figure 33. Microhardness testing results for NC samples

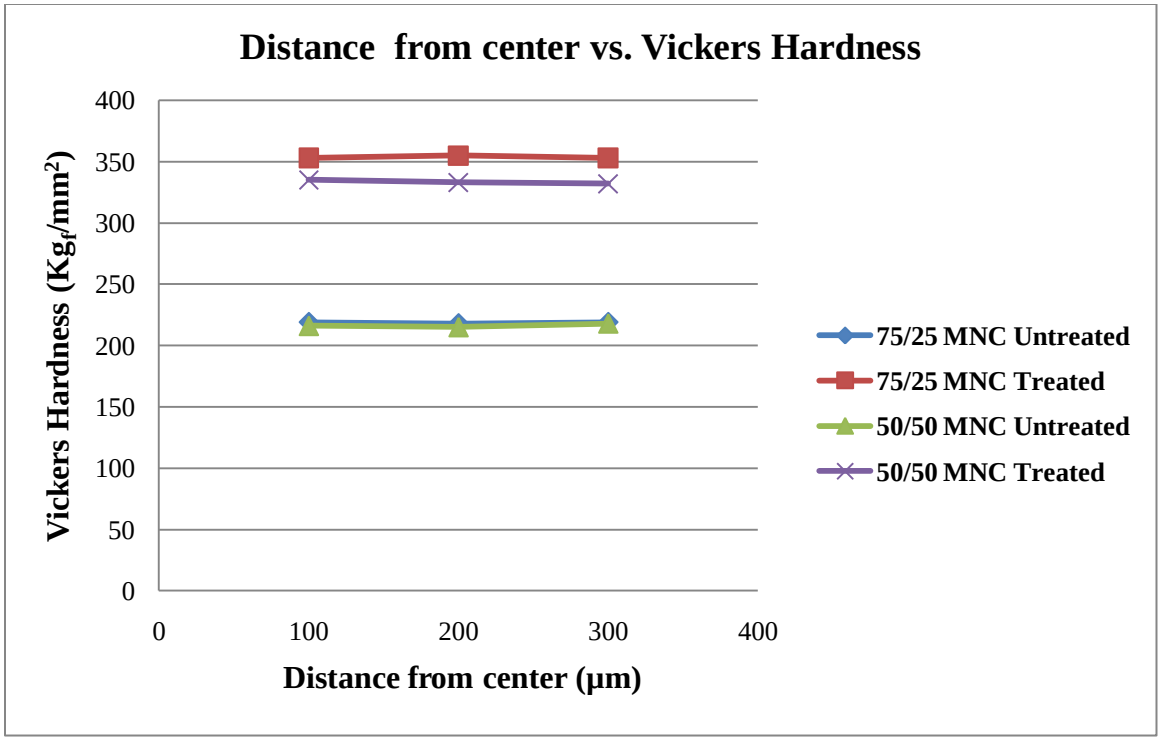

Figure 34. Microhardness testing results for MNC samples

It was hypothesized that the difference in hardness between the micro and nano powders was affected by different factors. The first being the particle size of the powders. The micro particles would have been able to absorb more of the shockwave during the LSP process that would result in larger compressive residual stresses; this explains the reason for the larger increase in hardness of the MC samples. Also, the grain coarsening that was seen in the NC and MNC was not found in the MC sample. Finer grains result in a larger hardness value. As mentioned previously coarsening could have been attributed to two different mechanisms dependent on the strength of the bonds between the particles. The agglomerates found in the nano powders could have attributed to the similar results in hardness seen in the MC samples since typical sizes are around 1 µm,

but they could have caused the coarsening as mentioned previously which lowered the hardness value.

Lastly, it should be noted that according to studies done by different research groups, porosity in YSZ will affect its mechanical properties (Gain, Song and Lee, 2006; Jang and Matsubara, 2005). Both research groups concluded that the higher the porosity in the YSZ, the lower the value in hardness. The hardness values of the MC, NC and MNC samples were lower than the bulk density value of YSZ of 1300 Kg_f/mm^2. This means the samples must have had a significant amount of porosity. Higher porosity should have been displayed in the MC samples since the size of the particles will affect the way that they pack together in a certain amount of space. However, due to nanopowders being composed of agglomerates similar porosity values could have been displayed. The data collected by Jang's research group indicates 20-25% porosity would have been seen in the MC, MNC and NC samples. However, these percentages could vary because of the difference in mole percentage of Y_2O_3. Jang's group used ZrO_2-4 % mole Y_2O_3 for their coatings however this research used ZrO_2-8 % mole Y_2O_3 compacts.

Hasanuzzaman's research group sintered two types of nano YSZ powder (Tosoh and Technox) compacts at high temperatures. Almost full density was achieved by using isothermal ramping and single dwell time sintering (Hasanuzzaman, Rafferty, Olabi and Prescott, 2008). However, such an approach is rarely optimal in terms of grain size and it was discovered one of the powders experienced complete shrinkage during isothermal sintering (Hasanuzzaman *et al*., 2008). The sintered compacts displayed a hardness range of 11 to 12.5 GPa. For both powders, hardness increased with increasing sintering temperature. The fracture toughness of the Tosoh powders decreased almost linearly

with increasing temperature compared to the Technox powders that led to maximum fracture toughness with two-step sintering (Hasanuzzaman *et al*., 2008). Table 14 lists the results of Hasanuzzaman's research group for both Tosoh and Technox powders.

Table 13. Density, hardness and fracture toughness values (Hasanuzzaman *et al*., 2008)

Sintering Temp (°C)	*Green Density % D_{th} Tosoh*	*Sintered Density % D_{th} Tosoh*	*Green Density % D_{th} Technox*	*Sintered Density % D_{th} Technox*	*Vickers Hardness Tosoh (GPa)*	*Vickers Hardness Technox (GPa)*	*Fracture Toughness Tosoh K_{IC} (MPa $m^{1/2}$)*	*Fracture Toughness Technox K_{IC} (MPa $m^{1/2}$)*
1350	40.11	97.40	40.75	94.67	11.67 ± 0.30	10.94 ± 0.34	5.49 ± 0.34	5.14 ± 0.25
1400	41.38	98.95	41.98	96.89	12.54 ± 0.23	11.48 ± 0.21	4.88 ± 0.28	5.08 ± 0.23
1450	40.94	99.44	40.99	97.57	12.30 ± 0.24	12.37 ± 0.37	4.97 ± 0.25	4.82 ± 0.26
1500	40.96	99.31	40.88	98.05	12.57 ± 0.17	11.97 ± 0.39	4.20 ± 0.38	5.47 ± 0.34
1550	–	–	40.68	99.11	–	12.19 ± 0.31	–	5.20 ± 0.26

Sintering offers a great opportunity to increase the hardness of nano YSZ powders (Hasanuzzaman *et al*., 2008). Nano powders have unique mechanical properties in strength, modulus and toughness as mentioned previously (Gutsch *et al*., 2004). Combining thermal sintering and LSP as a two-step process could hold promise for further increase in the mechanical properties of both micro and nano YSZ.

4.3 Thermal Conductivity Results

Thermal conductivity measurements were done for the samples from trial 3 that include: MC, NC, 50/50 and 75/25 MNC. Thermal conductivity test results are shown in Table 14.

Table 14. Thermal conductivity results

Sample	L (mm)	W (mm)	H (mm)	R (Ohm)	I (mA)	F (Hz)	$\alpha \times 10^7$ (m^2/s)	K (W/m·K)
MC	5.45	0.58	0.56	608.66	3.00	0.02	7.29	1.06
	5.45	0.58	0.56	608.66	3.00	0.02	7.14	1.04
	5.45	0.58	0.56	608.66	4.00	0.02	6.59	0.96
	5.45	0.58	0.56	608.66	5.00	0.01	7.08	1.03
NC	5.96	0.52	0.60	189.28	4.00	0.01	7.46	1.08
	5.96	0.52	0.60	189.28	5.00	0.01	6.16	0.89
	5.96	0.52	0.60	189.28	8.00	0.01	6.62	0.96
	5.96	0.52	0.60	189.28	10.00	0.01	6.51	0.94
50/50 MNC	3.00	0.47	0.43	1785.50	2.40	0.01	3.77	0.55
	3.00	0.47	0.43	1785.50	2.40	0.03	3.77	0.55
75/25 MNC	4.67	0.60	0.64	96.45	6.00	0.01	5.06	0.73
	4.67	0.60	0.64	96.45	6.00	0.02	5.45	0.79
	4.67	0.60	0.64	96.45	7.00	0.02	4.92	0.71
	4.67	0.60	0.64	96.45	8.00	0.02	5.06	0.73

(L-length, W-width, H-height, R-electrical resistance, I-current used for measurement, F-Frequency used for measurement, α-thermal diffusivity, k-thermal conductivity)

The 50/50 MNC had the lowest thermal conductivity average of 0.55 W/m·K while the MC had the highest at 1.02 W/m·K. These values are lower than the thermal conductivity of bulk YSZ which is 2 W/m·K. The MNC samples showed that combining the micro and nano powders greatly lowers the thermal conductivity of the YSZ compacts. These ceramics could be used for applications that require low thermal conductivity.

The reduction in thermal conductivity in MNC is attributed to the presence of nanoparticles at the pores that limit the mean free paths of phonons and photons. Thermal conductivity of YSZ is both a phonon and photon scattering phenomena. Creating atomic and nanoscale features such as vacancies, dislocations, grain boundaries and strain fields

(via nanoparticles) significantly reduce the mean free paths for phonons and photons and thereby lower thermal conductivity.

YSZ is intrinsically an electronic insulator and hence heat transfer does not occur though electrons as in other crystalline solids. Heat is transported by lattice vibrations (phonons) and by radiation (photons) where the latter becomes dominant at high temperatures. Being a molecular solid, YSZ consists of optical and acoustic phonons of a spectrum of frequencies. The fundamental equation for phonon conductivity is displayed in equation 6 which includes; *C* which is specific heat per unit volume, *v* is speed and *l* is mean free path. *C* and *l* are functions of the frequency while *v* is constant (according to Debye theory).

Equation 6. Phonon Conductivity

$$\kappa = (1/3)Cvl$$

Point defects such as solute cations and oxygen vacancies reduce the contribution of the high frequency spectrum by scattering phonons as the fourth power of frequency (Klemens and Gell, 1998). Extended imperfections such as grain boundaries and voids scatter phonons at low frequencies. In addition, ions and atoms of differing radii also scatter phonons by locally distorting the bond length and introducing elastic strain fields into the lattice. Interaction between phonons can contribute to scattering although this phenomenon is independent of frequency. All these phonon conductivity reductions can be enhanced by *decreasing the average grain size as shown in Figure 35* (Klemens and Gell, 1998).

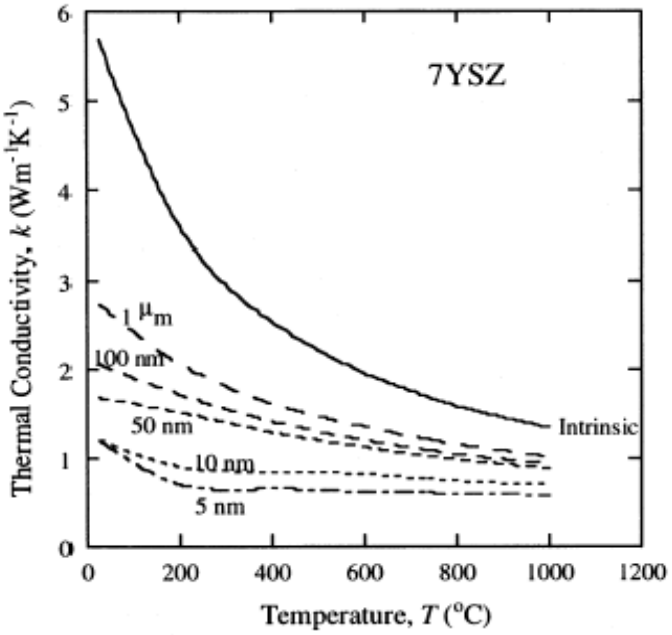

Figure 35. Theoretical thermal conductivity of ZrO_2-7%Y_2O_3 by grain size reduction (Klemens and Gell, 1998)

In order to achieve thermal conductivity <0.5 W/m K, nanometer sized grains and point defects are required for phonon conductivity while pores or dopants are needed to reduce the radiative component. Pores may be preferable to dopants, since they present a larger contrast in the index of refraction, provided they can be introduced in the right size. For example, recent innovations in YSZ are creating nanoporous microstructures (Gu, Lu, Haas and Wadley, 2001) and doping it with multicomponent rare-earth oxides (Zhu and Miller, 2004) to promote reduction in thermal conductivity, enabling greater temperature reductions and less cooling to the components. *In summary, applications that require low thermal conductivity, high thermal expansion, increased strength and toughness may consider the use of LSP coupled with micro/nanopowder mixture.*

4.4 Analytical Model

An analytical model for LSP described in (Ding and Ye, 2006) and reproduced in section 4 of the Appendix, is utilized to determine the various effects such as surface residual stress, plastic strain and plastically affected depth for MC and NC samples. The model is formulated based on the propagation of confined plasma below the transparent overlay and freely expanding plasma above the overlay. It considers that a portion of laser energy is used to develop pulse pressure and the remaining portion is used to create ionization. The governing equations included the effect of impedance of the different materials for the shock wave propagation. The energy balance model considered both volume change (elastic wave) and distortion (plastic wave) and employed wave propagation and elasticity equations. The following assumptions are made while applying the governing equations.

1) Duration of pulse pressure is the same as the pulse width of laser beam.
2) Bulk density of 6 g/cm^3 and Poisson's ratio of 0.31 of YSZ
3) Due to limited information on YSZ the dynamic yield strength is assumed to be equal to the flexural strength of bulk YSZ.
4) Bulk Young's modulus of YSZ (200 GPa) was used for the MC samples. However, due to the Young's modulus of nanomaterials depending on size, surface orientation, crystal orientation, and geometry (Gutsch *et al*., 2004; Sun and Zhang, 2003) compared to their bulk counterparts a lower Young's modulus was used. The 194 GPa Young's modulus was determined from Hasanuzzaman's research group who characterized nano YSZ powders (Hasanuzzaman, *et al.*, 2008).

5) Porosity of 30 % was assumed for MC and NC samples (Jang and Matsubara, 2005).
6) The assumed Density, Young's Modulus and Flextural Strength for bulk YSZ was adjusted using the rule of mixtures ($E_{YSZ} = \nu*E_{Bulk} + (1-\nu)*E_{Porosity} = 0.7*E_{Bulk}$) to account for the porosity.
7) It was assumed the samples had no initial stresses.
8) Shock velocity of 8.45 km/s for YSZ was assumed (Dolan and Ao, 2008)
9) Efficiency of the interaction α is assumed as 0.25 (Bethe *et al.*, 1997)
10) The theoretical spot size radius was used in the calculation of the surface residual stress.

The calculated Lamé's constants, Hugoniot elastic limit, elastic and plastic wave velocities of the MC and NC samples are listed in Table 15. The calculated surface residual stress, plastically affected depth and plastic surface strain of the MC and NC samples are listed in Table 16. The shock impedance (Z) for a water/YSZ interface was calculated as 3.15×10^5 g/cm^{2}s.

Table 15. Model Results 1

Sample	E (GPa)	μ (GPa)	λ (GPa)	σ_Y^{dyn} (MPa)	HEL (MPa)	C_{el} (m/s)	C_{pl} (m/s)
MC	140	53	87	630	1144	6797	5407
NC	136	52	85	630	1144	6695	5326

E=Young's Modulus, μ=Shear Modulus=E /[2(1+v)], λ=Lamé constant=Ev/[(1+v)(1-2v)], C_{el}=Elastic Wave Velocity=$[(\lambda+2\mu)/\rho]^{1/2}$, C_{pl}=Plastic Wave Velocity=$[(\lambda+2\mu/3)/\rho]^{1/2}$, HEL=$[(1-v)/(1-2v)]\sigma_Y^{dyn}$

Table 16. Model Results 2

Sample	Repetition Rate (Hz)	Peak Power Density (GW/cm^2)	P (GPa)	ε_p	L_p (mm)	σ_{surf} (MPa)
MC	5	1.89	4.18	0.0165	0.25	-128
MC	3	2.20	4.34	0.0173	0.26	-236
NC	5	1.89	4.18	0.0170	0.24	-101
NC	3	2.20	4.34	0.0179	0.25	-206

$P=0.01[\alpha/(2\alpha+3)]^{1/2}Z^{1/2}I_0^{1/2}$, $\varepsilon_P=[(-2HEL)/(3\lambda+2\mu)](P/HEL-1)$, $L_p=[(C_{el}*C_{pl}*\tau)/(C_{el}-C_{pl}][(P-HEL)/(2HEL)]$, $\sigma_{surf}=\sigma_0-[(\mu*\varepsilon_P*(1+v))/((1-v)\ )+\sigma_0][1-((4\sqrt{2})/\pi)(1+v)*L_P/(r\sqrt{2})]$

Model results indicate the MC samples experienced approximately 13% (5Hz) and 21% (3Hz) increase in compressive surface residual stresses deeper in the material compared to NC. The plastically affected depths for the samples indicate the penetration of the LSP process reached 25% of the 1 mm thick compacts. The NC samples had approximately 3% increase in plastic strain compared to the MC samples which indicates more plastic deformation in the NC samples. Lowering the repetition rate from 5 to 3 Hz increases the pulse pressure, plastically affected depth and surface plastic strain by 4% for both MC and NC, while the surface residual stresses increased by 85% (MC) and 104% (NC). The calculated pulse pressure is approximately 40% higher than the pressure estimated from Figure 6.

Higher compressive stresses would explain the quality difference seen between the samples that used different parameters. During the experimental process the 5 Hz samples turned out better compared to the 3 Hz samples that were rough and damaged as seen in the SEM images. SEM results indicated small surface cracks on the untreated surface of the MC sample, applying these high stresses deep into the material could have attributed to the surface cracking that was seen in the treated surface. The smaller plastically affected depth and lower surface residual stresses in the NC samples could have attributed to the smoother surfaces. The powders must have a limit on the amount of stress they can withstand in their compacted form before they start to fracture.

Model results agree with the hypothesizes that laser shock waves create a compressive stress pattern that causes plastic deformation of the particles and a large increase in the concentration of vacancies on the surface of the particles; this highly defective surface coupled with a high surface mobility of nanoparticles is responsible for the mass transport. The higher surface plastic strain of the NC samples confirms this.

The model supports the hardness data that was measured. MC samples experienced higher stresses deeper in the material compared to the NC samples which explains the larger increase in hardness of 64% for MC compared to the 44% of the NC samples.

Chapter 5. Conclusion

Mechanical (non-thermal) sintering behavior of yttria stabilized zirconia (YSZ) powder compact was investigated as a function of particle size. Laser shock wave consolidation of micro and nano YSZ compacts using a Nd:YAG laser at 532 nm wavelengths and two peak power densities was performed. Cubic crystalline form of ZrO_2 containing 8 mole% Y_2O_3 powders of the nominal size 16 µm and 45 nm were acquired. Five samples consisting of different proportions of micro and nano powders were uniaxially cold-pressed by applying 69 MPa of pressure to produce green compacts. These compacts were then subjected to a novel laser shock peening (LSP) process using a water-confining medium and black paint ablative coating for densification. Results of the experiment are summarized below.

- Micropowder compacts (MC) excessively cracked and chipped while nanopowder compact (NC) and mixtures of micro/nanopowder compacts (MNC) underwent sintering without crack formation.
- SEM imaging displayed evidence of stress-assisted material removal and surface disruption in NC samples, making their surfaces much rougher than those of MC samples. Also, a grain coarsening effect was shown in NC and MNC as compared to MC.
- Microhardness testing results indicated MC exhibiting a much higher increase in hardness over NC and MNC samples. For example, a 64 % increase in hardness was noted in MC compared to a 44 % increase in NC.
- Thermal conductivity measurements indicated that the MNC has approximately half the thermal conductivity of the MC. The reduction in thermal conductivity in MNC

is attributed to the presence of nanoparticles at the pores that limit the mean free paths of phonons and photons.

- Analytical model results indicated higher surface residual stresses deeper in the material for MC compared to NC. The NC samples had higher plastic strain compared to the MC samples which indicates more plastic deformation in the NC samples. The plastically affected depths for the samples indicate the penetration of the LSP process reached over 25% of the 1 mm thick compacts. Lowering the repetition rate from 5 to 3 Hz increases the pulse pressure, plastically affected depth and surface plastic strain by 4% for both MC and NC, while the surface residual stresses increased by 85% (MC) and 104% (NC).
- Overall an improved densification was obtained in NC and MNC samples.

Chapter 6. Future Work

Laser shock wave consolidation of micro and nano YSZ compacts has proven to be successful. Further investigation of the effect of LSP on YSZ powders must be conducted to further validate its applications to create high density parts. Listed below is the future work for continuation of this project.

1) Combining thermal sintering and LSP as a two-step process
2) Variation of MNC by 5% increments
3) Variation of porosity in MC, NC and MNC samples
4) Variation of size of MC, NC and MNC samples
5) Stress and strain measurements of the samples to compare with model results
6) Measurement of fracture toughness, flexural strength, yield strength and compressive strength of micro and nano YSZ powders
7) Applying coatings to prevent cracking and rupturing of the surface
8) Finite element simulation of MC, NC and MNC samples

References

1. Ballard, P., et al., *Residual Stresses Induced by Laser-Shocks*. Journal de Physique IV, 1991. **1**: p. C3487-494
2. Berthe, L., et al., *Shock waves from a water-confined laser-generated plasma*. Journal of Applied Physics, 1997. **82**: p.2826-2832
3. Boustie, M., et al., *Laser Shock Waves: Fundamentals and Applications*, 1st International Symposium on Laser Ultrasonics: Science, Technology and Applications, Montreal, Canada, July 16-18, 2008.
4. Bouvier, P., V. Dmitriev and G. Lucazeau, *The high-pressure phase sequence in nano-crystalline zirconia*. The European Physical Journal B, 2003. **35**: p. 301-309
5. Caslaru, R., et al., *Fabrication and Characterization of Micro Dent Array Produced by Laser Shock Peening on Alminum Ssurfaces*. Transactions of NAMRI/SME, 2009. **37**: p. 159-165
6. Che, Z., et al., *Numerical and Experimental Study of Microscale Laser Shock Processing Using Excimer Laser*. Proceedings of the 2009 4th IEEE International Conference on Nano/Micro Engineered and Molecular Systems, Shenzhen, China, January 5-8, 2009. nems, p. 256-269
7. Cheng, G. J., et al., *Plastic Deformation in Silicon Crystal Induced by Heat-Assisted Laser Shock Peening*. Journal of Manufacturing Science and Engineering, 2008. **130**: p. 011008 - 1-5

8. Clauer, A., *Laser shock peening for fatigue resistance*, in *Surface Performance of Titanium*, J. Gregory, H. Rack and D. Eylon, Eds. 1996, TMS, Warrendale, PA, USA, p. 217-230

9. Dahotre, N.B. and S.P. Harimkar, *Laser Fabrication and Machining of Materials.* New York: Springer Science, 2008

10. Ding, K. And L. Ye, *Laser shock peening: Performance and process simulation*. Boca Raton, FL: CRC Press LLC, 2006

11. Dolan, D. H. and T. Ao, *Cubic zirconia as a dynamic compression window*. Applied Physics Letters, 2008. **93**: p. 021908-1-3

12. Drings, H., U. Brossmann and H. Schaefer, *Preparation of crack-free nanocrystalline yttria-stabilized zirconia*, Physica Status Solidi (RRL), 2007. **1**: p. 3-8

13. Dubrujeaud, B. and M. Jeandin, *Cladding by laser shock processing*. Journal of Materials Science Letters, 1994. **13**: p. 773-775

14. Fabbro, R., et al., *Physical study of laser-produced plasma in confined geometry*. Journal of Applied Physics, 1990. **68**: p. 775-784

15. Gain, A. K., H. Song and B. Lee, *Microstructure and mechanical properties of porous yttria stabilized zirconia ceramic using poly methyl methacrylate powder*. Scripta Materialia, 2006. **54**: p. 2081-2085

16. Garrido, L. B., et al., *Hardness and fracture toughness of mullite-zirconia composites obtained by slip casting*. Material Science and Engineering A, 2006. **419**: p. 290-296

17. Gu, S. et al., *Thermal Conductivity of Zirconia Coatings with Zig-Zag Pore Microstructures*. Acta Materialia, 2001. **49**: p. 2539-2547

18. Guo, J., X. Wang and T. Wang, *Thermal characterization of microscale conductive and nonconductive wires using transient electrothermal technique*. Journal of Applied Physics, 2007. **101**: p. 063537-1-7

19. Gutsch, A., et al., *Gas-Phase Production of Nanoparticles*. KONA, 2002. **20**: p. 24-37

20. Hasanuzzaman, M., A. Rafferty, A. Olabi and T. Prescott. *Sintering and characterization of nano-sized yttria-stabilized zirconia*. International Journal of Nanoparticles, 2008. **1**: p. 50-65

21. Hass, D., *Directed Vapor Deposition of Thermal Barrier Coatings.* Ph.D. Dissertation, University of Virginia, 2000.

22. Hong, Z. And Y. Chengye, *Laser shock processing of 2024-T62 aluminum alloy*. Materials Science and Engineering, 1998. **A257**: p. 322-327

23. Hurevich, V., I. Smurov and L. Pawlowski, *Theoretical study of the powder behavior of porous particles in a flame during plasma spraying*. Surface and Coatings Technology, 2002. **151-152**: p. 370-376

24. Jang, B. and H. Matsubara, *Influence of porosity on hardness and Young's modulus of nanoporous EB-PVD TBCs by nanoindentation*. Materials Letters, 2005. **59**: p. 3462-3466

25. Kalinnikov, A.E. and L. Vakhrusheva, *Estimation of residual stresses in a powder compact pressed in a rigid die*. Poroshkovaya Metallurgiya, 1985. **7**: p. 16-20

26. Kim, H., *Low Temperature Sintering Of Nanosized Ceramic Powder: YSZ-Bismuth Oxide System*. Ph.D. Dissertation, The Ohio State University, 2004.

27. Klemens, P. G., *Thermal Conductivity of ZrO_2*, in *Thermal Conductivity*, K. Wills, R. Dinwiddie, R. Graves, Eds. 1993, Technomics, Lancaster, PA, **23**: p. 209-220

28. Klemens, P. G. and M. Gel, *Thermal Conductivity of Thermal Barrier Coatings*. Material Science and Engineering A, 1998. **245**: p. 143–149

29. Kruusing, A., *Underwater and water-assisted laser processing: Part 1—general features, steam cleaning and shock processing*. Optics and Lasers in Engineering, 2004. **41**: p. 307–327

30. Mashimo, T., et al., *Yielding and phase transition under shock compression of yttria-doped cubic zirconia single crystal and polycrystal*. Journal of Applied Physics, 1995. **77**: p. 5060-5068

31. Molian, P., R. Molian and R. Nair, *Laser shock wave consolidation of nanodiamond powders on aluminum 319*. Applied Surface Science, 2009. **255**: p. 3859–3867

32. Montross, C. S., et al., *Laser shock processing and its effects on microstructure and properties of metal alloys a review*. International Journal of Fatigue, 2002. **25**: p. 1021-1036

33. Nakaso, K., et al., *Evaluation of the change in the morphology of gold nanoparticles during sintering*. Journal of Aerosol Science, 2002. **33**: p. 1061-1074

34. Othman, S. Z., S. Ramesh and W. Teng, *Sintering of Commercial Yttria-Stabilized Zirconia*. Engineering e-Transaction, 2006. **1**: p. 14-18

35. Pinto, C., et al., *Measurement of Thermophysical Properties of Ceramics by the Flash Method*. Brazilian Archives of Biology and Technology, 2006. **48**: p. 31-39

36. President's Council of Advisors on Science and Technology, *The National Nanotechnology Initiative at Five Years: Assessment and Recommendations of the National Nanotechnology Advisory Panel*, 2005. p. 1-50

37. Rubio-Gonzalez, C., et al., *Effect of an absorbent overlay on the residual stress field induced by laser shock processing on aluminum samples*. Applied Surface Science, 2006. **252**: p. 6201-6205

38. Rubio-Gonzalez, C., et al., *Effect of Laser Shock Processing on Fatigue Crack Growth and Fracture Toughness of 6061-T6 Aluminum Alloy.* Materials Science and Engineering - A, 2004. **386**: p. 291-295.

39. Peleg, M., M. Normand and M. Corradini, *Interactive software for calculating the principal stresses of compacted cohesive powders with the Warren-Spring equation*. Powder Technology, 2010. **197**: p. 268-273

40. Peyre, P., et al., *Laser shock processing of aluminium alloys. Application to high cycle fatigue behaviour*. Materials Science and Engineering - A, 1996. **210**: p. 102-113

41. Sealy, M. P. And Y. Guo, *Fabrication and Finite Element Simlation of Micro-Laser Shock Peening for Micro Dents*. International Journal for

Computational Methods in Engineering Science and Mechanics, 2009. **10**: p. 134-142

42. Smith, P.R., et al., *Effect of Power Density and Pulse Repetition on Laser Shock Peening of Ti-6AI-4V*. Journal of Materials Engineering and Performance, 2000. **9**: p. 33-37

43. Sun, C. T. and H. Zhang, *Size-dependent elastic moduli of platelike nanomaterials*. Journal of Applied Physics, 2003. **9**: p. 1212-1218

44. Warren, A.W., Y. Guo and S. Chen, *Massive Parallel Laser Shock Peening: Simulation, Analysis, and Validation.* International Journal of Fatigue, 2008. **30**: p. 188-197.

45. Yilbas, B. S. and A. Arif, *Laser shock processing of aluminum: model and experimental study*. Journal of Physics D: Applied Physics, 2007. **40**: p. 6740-6747

46. Zhang, W. and Y. Yao, *Improvement of laser induced residual stress distributions via Shock Waves*. Journal: Proceedings of the Laser Materials Processing Conference; ICALEO, 2000. **89**: p. 183-192

47. Zhang, W. and Y. Yao, *Microscale Laser Shock Peening-Modeling, Testing, and Microstructure Characterization*. Journal of Manufacturing Processes, 2001. **3**: p. 128-143

48. Zhang, W. and Y. Yao, *Microscale Laser Shock Processing of Metallic Components*. Journal of Manufacturing Science and Engineering, 2002. **124**: p. 369-378

49. Zhang, W., Y. Yao and I. Noyan, *Microscale Laser Shock Peening of Thin Films, Part 1 Experiment Modeling and Simulation*. Journal of Manufacturing Science and Engineering, 2004. **126**: p. 10-17

50. Zhang, Y.K., et al., *Effect of laser shock processing on the mechanical properties and fatigue lives of the turbojet engine blades manufactured by LY2 aluminum alloy*. Materials and Design, 2009. **30**: p. 1697-1703

51. Zhao, Q., A. Boxman and U. Chowdry, *Nanotechnology in the Chemical Industry – Opportunities and Challenges*. Journal of Nan particle Research, 2003. **5**: p. 567-572

52. Zhu, D. and R. Miller, *Development of Advanced Low Conductivity Thermal Barrier Coatings*. International Journal of Applied Ceramic Technology, 2004. **1**: p. 86-94

Appendix

1. Equipment Operating Procedures

1.1 Laser Operating Procedures

1. Plug in the power cord.
2. Turn on the main power switch.
3. Turn the laser to I.
4. Press the start button.
5. Keep the Q-SW Mode in long pulse.
6. Increase lamp energy button to full to see the long pulse beam
7. If beam is visible lower lamp energy.
8. Switch the Q-SW Mode to Q-SW.
9. Variable Repetition Rate and Q-SW Delay can now be used to change laser parameters.
10. Reduce lamp energy to zero after experiment is finished.
11. Cool down the lamp/rod for 5-10 mins.
12. Turn Laser key switch off.
13. Turn main power off.
14. Unplug the Power Cord

1.2 Newmark Systems XYZ Positioning Table

1. Turn the switch on the back of the motherboard on.
2. Turn the switch on the front of the motherboard on, this will turn on a green light.

3. Open Newmark Systems icon on the computer.
4. Initial position when the motherboard is turned on will be considered Home.
5. Make sure text on the command prompt shows connection to the motherboard.
6. Use a command script window to type desired code and send to the table.
7. For specific commands see the manual provided.
8. Set table to original position after use.
9. Turn the switch on the front of the motherboard off., this will turn off the green light.
10. Turn the switch on the back of the motherboard off.

1.3 Powder Compaction and Press Operating Procedures

1. Measure desired weight powder.
2. Insert the shorter rod into the bottom of the die.
3. Pour the measured powder carefully into the top of the die.
4. Insert the longer rod into the top of the die.
5. Make sure lever is fully retracted on the press.
6. Place the die in the compartment directly under the press bar.
7. Pull the lever down until the bar reaches the top surface of the longer rod.
8. Apply desired force on the die.
9. Retract lever until the die is released.
10. Apply force to the top of the longer rod to release the shorter rod.
11. Carefully tap the top of the die to release the compacted disk.

1.4 Hardness Testing Operating Procedures

1. Turn on the Wilson Tukon hardness tester
2. Lower stage enough to place sample on the stage
3. Raise stage until surface becomes visible
4. Focus surface until details are visible
5. Apply desired force on the sample
6. Use the horizontal and vertical knobs to align cursor lines with indentation marks on the sample surface
7. After cursors are aligned a measurement should be displayed on the machine
8. Press calculate and desired hardness will be displayed on the monitor

1.5 Sputter Coating Operating Procedures

1. Turn on the Argon gas using the main knob A first and followed by the small knob B on the gas cylinder.
2. Turn on the cold water for a low stream (about ¼ turn).
3. Place sample into chamber and align it under the target. Use the proper sample holders designed for gold sputter.
4. Turn on sputter unit by pressing Power button.
5. Turn on pump by pressing the Pump button, after a few seconds Interlock light should come on.
6. After the pressure has dropped to at least 0.1 mbar, press the Start button.
7. Wait 10-15 seconds, pressure should equilibrate to 0.3–0.4 mBar.

8. After the pressure has come to equilibrium around 0.3 mBar, turn on the high tension by pressing the H. T. button.
9. Slowly turn up the voltage all the way to 10.
10. Sputter for 1-2 minutes, then slowly turn down the voltage to 0, and switch the H. T. button off.
11. Vent the chamber by pressing the Vent button.
12. Turn off the water and the Argon using the same knobs used in step 1.
13. Turn off sputter unit by pressing the power button and collect sample.
14. Make sure chamber is sealed when finished to minimize contamination.

2. Experimental Procedures

1. Use sterile gloves and tools
2. Clean out glass container with distilled water
3. Tape the bottom side of the sample to the vertical stand on the glass container
4. Fill the container with water until the sample sits 2 mm from the surface
5. Place glass container on the xyz table
6. Attach air hose to the side of the glass container
7. Follow laser procedures to power up the laser
8. Line up laser beam with the outside edge of the sample
9. Set desired repetition rate
10. Slowly increase the power
11. Start command script program to move xyz table
12. After program ends slowly decrease the power
13. Place glass container on a stable surface
14. Carefully remove the sample

3. Command Script

3 Hz

```
AA VL0.15,0.15,0.15;
LS4
AA MR0,8,0; GO
AA MR0.5,0,0; GO
AA MR0,-8,0; GO
AA MR0.5,0,0; GO
LE;
```

5 Hz

```
AA VL0.5,0.5,0.5;
LS4
AA MR0,8,0; GO
AA MR0.5,0,0; GO
AA MR0,-8,0; GO
AA MR0.5,0,0; GO
LE;
```

4. Analytical Model Background

During LSP, the heated zone of the coating on the metal surface is vaporized, reaching temperatures up to 10,000 °C and is transformed into plasma by ionization (Ding and Ye, 2006). A high pressure on the material surface can be generated as a result of the blowing off of the high-temperature plasma. Consequently, shockwaves are produced inside the material and depicted in Figure 36.

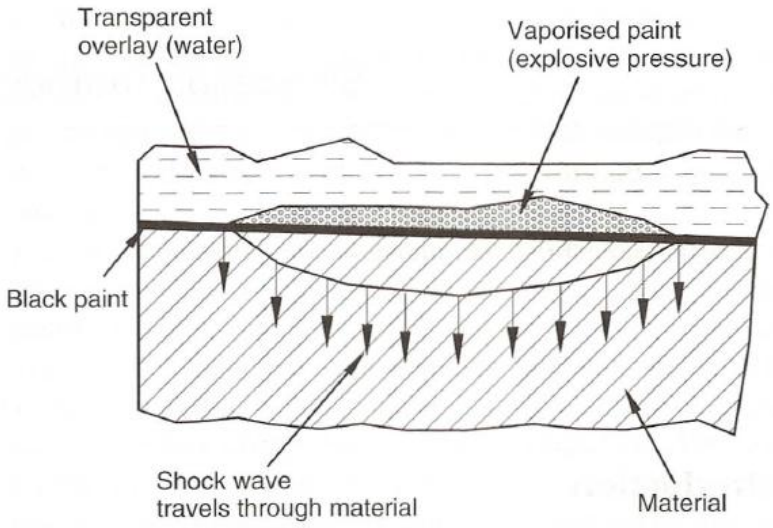

Figure 36. Geometry of a model in the confined ablation mode (Ding and Ye, 2006)

A physical model to predict the pulse pressure as a function of laser power density was used, characterizing the difference between the confined plasma below the transparent overlay and the freely expanding plasma above the overlay (Ding and Ye, 2006). Figure 37 depicts the confined plasma in the physical model. The model indicates that pressure is strong enough to generate two shockwaves in the two mediums, which

results in the wall displacement being affected by the fluid motion of the two shockwaves propagating inside the two materials. The figure displays the two fluid velocities u_i (i = 1, 2) behind the two shock waves given by the shock-wave relation $P = Z_i * u_i = \rho_i * D_i * u_i$. Where Z_i, ρ_i and D_i are the shock impedance, density and shock velocity, the index i represents the different materials.

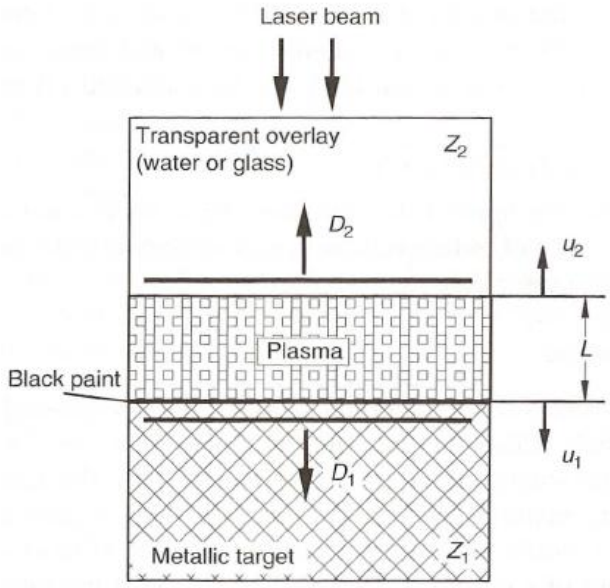

Figure 37. Geometry of a model in the confined ablation mode (Ding and Ye, 2006)

This evaluation indicates; pulse pressure (P), thickness (L) between the material surface and the overlay, expansion velocity (V) and laser power density (I), of the plasma during laser irradiation are calculated as a function of time (t) using equations 7 and 8 (Ding and Ye, 2006).

Equation 7. Laser Power Density

$$\boldsymbol{I(t) = P(t)\frac{dL(t)}{dt} + \frac{3}{2\alpha}\frac{d}{dt}[P(t)L(t)]}$$

Equation 8. Expansion Velocity

$$V(t) = \frac{dL(t)}{dt} = \left(\frac{1}{Z_1} + \frac{1}{Z_2}\right) P(t)$$

During constant laser power density (I_0), the scaling law for the pulse pressure is calculated using equation 9 (Ding and Ye, 2006). P is defined as the peak pulse pressure, α is the efficiency of the interaction and Z is the combined shock impedance defined as $Z = 2(Z_1 * Z_2) / (Z_1 + Z_2)$. The total energy ($E_T$) from the laser source is converted into two parts during the interaction. The first part of the energy (αE) establishes the pulse pressure while the second part ($[1 - \alpha] * E$) generates and ionizes the plasma; α is typically between 0.2-0.5 (Ding and Ye, 2006).

Equation 9. Pulse Pressure

$$P = 0.01\sqrt{\frac{\alpha}{2\alpha + 3}}\sqrt{Z}\sqrt{I_0}$$

Based on the confined ablation mode, an LSP process may be described by a two step sequence: (1) the rapid plasma expansion creates sudden uniaxial compression on the irradiated area and dilation of the surface layer and (2) the surrounding material reacts to the deformed area, generating a compressive stress field, shown in Figure 38 (Ding and Ye, 2006).

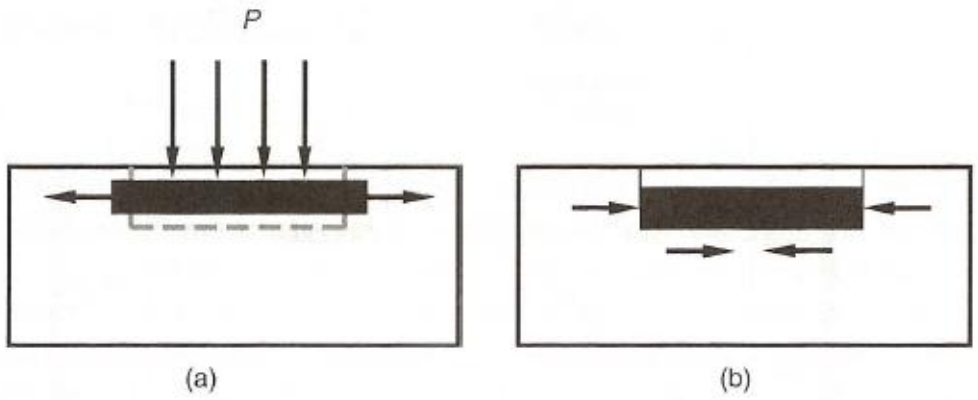

Figure 38. Generation of compressive residual stresses with LSP. (a) Stretching of impact area during the interaction, (b) Recovery of the surrounding material after laser pulse is switched off (Ding and Ye, 2006)

To determine the compressive residual stresses created from the LSP process the plastically affected depth and the surface plastic strain must be evaluated. The plastic strain depends only on the depth (*z)*, in a one-dimensional model. The absolute value of the plastic strain is a decreasing function of *z*. On the surface of the material, ignoring work hardening and viscous effects, the plastic strain (ε_P), depends only on the magnitude of the pulse pressure (*P*) as displayed in Figure 39 (Ding and Ye, 2006). The surface plastic strain (ε_P), is calculated using equation 10, where *HEL* is the Hugoniot elastic limit, *P* is the peak pressure, λ and μ are the Lamé's constants.

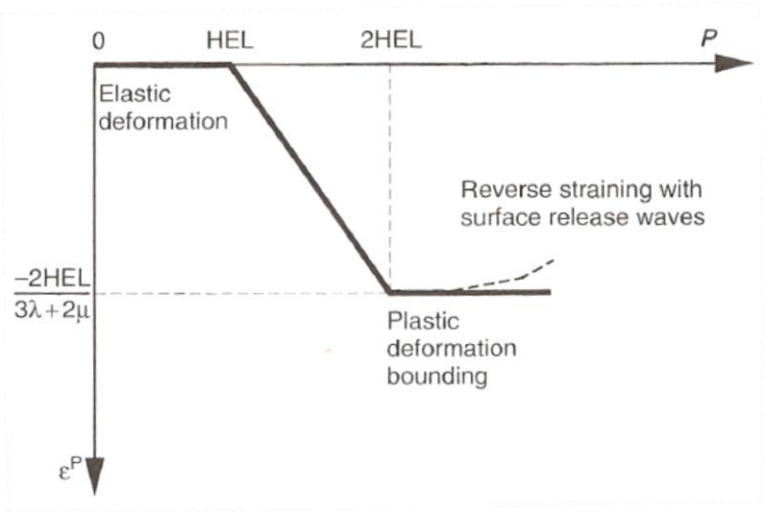

Figure 39. Plastic strain induced by LSP as a function of peak pressure (Ding and Ye, 2006)

Equation 10. Surface Plastic Strain

$$\boldsymbol{\varepsilon_P = \frac{-2HEL}{3\lambda + 2\mu}\left(\frac{P}{HEL} - 1\right)}$$

When considering deformation of a material under applied loads, the stress-strain relationship governing behavior of an isotropic elastic solid can be expressed by the 'generalized Hooke's law': where the dilation ($\Delta = \varepsilon_{xx} + \varepsilon_{yy} + \varepsilon_{yy}$) is the change in volume of a unit cube and the two elastic constants, λ and μ are the Lamé's constants (Ding and Ye, 2006). In terms of Young's modulus (E), Poisson's ratio (v), and shear modulus (G), the two constants can be calculated using equations 11 and 12.

Equation 11. Lamé Constant μ

$$\boldsymbol{\mu = G = \frac{E}{2(1+v)}}$$

Equation 12. Lamé Constant λ

$$\boldsymbol{\lambda = \frac{Ev}{(1+v)(1-2v)}}$$

Stress waves transmitted through an elastic-plastic material can be separated into two distinct waves, an elastic wave with a magnitude in the Hugoniot elastic limit (*HEL*) and a plastic wave (Ding and Ye, 2006). The *HEL* depends on the material properties and is calculated using equation 13: where σ_Y^{dyn} is the dynamic yield strength at a high strain rate (about 10^6 s^{-1}) and *v* is Poisson's ratio. It is assumed in equation 11, that the pressure increases linearly between 1 × *HEL* and 2 × *HEL*. If *P*, is equal to 2 × *HEL*, the surface plastic strain is saturated (Fig. 39). However, if *P* is greater than 2 × *HEL* and less than 2.5 × *HEL*, no further plastic deformation occurs (Ding and Ye, 2006).

Equation 13. Hugoniot Elastic Limit

$$\boldsymbol{HEL = \frac{\lambda + 2\mu}{2\mu}\sigma_Y^{dyn} = \frac{(1-v)\sigma_Y^{dyn}}{(1-2v)}}$$

In order to determine the residual stress field in the material, the plastically affected depth (L_P), for any given shock condition must be calculated. L_P is a function of temporal profile of pulse pressure using the characteristic diagram of stresses (Ding and

Ye, 2006). L_P is expressed as equation 14 where; C_{el} and C_{pl} are the elastic and plastic wave velocities in the material, τ is the duration of pulse pressure. For overlays with low acoustic impedance, the pressure duration is nearly equal to the laser pulse duration (Ding and Ye, 2006). C_{el} and C_{pl} are calculated using equations 15 and 16 where ρ is the density of the material.

Equation 14. Plastically Affected Depth

$$L_p = \left(\frac{C_{el}C_{pl}\tau}{C_{el}-C_{pl}}\right)\left(\frac{P-HEL}{2HEL}\right)$$

Equation 15. Elastic Wave Velocity

$$C_{el} = \sqrt{\frac{\lambda + 2\mu}{\rho}}$$

Equation 16. Plastic Wave Velocity

$$C_{pl} = \sqrt{\frac{\lambda + 2\mu/3}{\rho}}$$

The residual stress field induced by LSP can be determined through the characteristic diagrams of stresses and material velocities. However, given the time, $t = +\infty$, after the impact, the residual stress field can be deduced by those characteristic diagrams (Ding and Ye, 2006). When the surface plastic strain and the plastically affected depth are both know, the surface residual stress can be calculated for a square

laser spot using equation 17 or for a circular laser spot using equation 18. Both equations use σ_0 as the initial residual stress. However, a is the edge of a square laser spot and r is the radius in a circular laser spot.

Equation 17. Surface Residual Stress (Square Laser Spot Size)

$$\boldsymbol{\sigma_{surf} = \sigma_0 - \left[\frac{\mu\varepsilon_P(1+v)}{(1-v)} + \sigma_0\right]\left[1 - \frac{4\sqrt{2}}{\pi}(1+v)\frac{L_P}{a}\right]}$$

Equation 18. Surface Residual Stress (Circular Laser Spot Size)

$$\boldsymbol{\sigma_{surf} = \sigma_0 - \left[\frac{\mu\varepsilon_P(1+v)}{(1-v)} + \sigma_0\right]\left[1 - \frac{4\sqrt{2}}{\pi}(1+v)\frac{L_P}{r\sqrt{2}}\right]}$$